On the conditions for lower crustal convective instability.

M. Jull and P. B. Kelemen

Woods Hole Oceanographic Institute, Woods Hole MA 02543, USA;
jull@whoi.edu, pkelemen@whoi.edu;
Tel.(508) 289-3248 Fax.(508) 457-2183

Submitted to *Journal of Geophysical Research*

Abstract

A fundamental problem in understanding the formation of continental crust is that the majority of magmas erupted on earth are basaltic, and yet the continents do not have a basaltic bulk composition. Continental crust is thought to be formed as a result of arc magmatism, but many of the lavas produced in these settings are basaltic, whereas more silicic lavas are commonly evolved, with lower Mg#'s than the continental crust. Mixing of end-member compositions, via magma mixing or in mechanical, tectonic juxtaposition, can produce the composition of the bulk continental crust, but some process is required to remove the cumulates and residues formed during generation of the silicic, "granitic" end-member. We consider convective instability of dense mafic and ultramafic lower crust as a means to remove mafic residues of basalt differentiation in order to produce end-member compositions that can mix to form the bulk composition of the continental crust. Using a range of lower crustal and mantle bulk compositions, ranging from mafic and ultramafic cumulates to primary liquid compositions, we calculated the subsolidus phase assemblage and resulting density. The results show that densities of likely lower crustal lithologies can exceed those of the mantle (by $\sim 50 - 250$ kg/m^3) , but the density contrast is a strong function of composition, temperature, and pressure. For a "cold" geotherm with a Moho temperature of 300 °C, relevant to cratonic settings, densities of all of the lower crustal compositions that we considered, except granulite, exceed the density of the underlying mantle at pressures as low as 0.8 GPa. For a "hot" geotherm with a Moho temperature in the range of 800-1000 °C, the density of the lower crust is much more variable, with gabbroic and granulite compositions generally less dense than the mantle, but "arc gabbronorite" and ultramafic cumulate compositions denser than the mantle at pressures similar to that for the "cold" geotherm. Instability times calculated for a two-dimensional Rayleigh-Taylor convective instability, where a dense lower crustal layer sinks into a less-dense mantle, show that high temperatures (greater than 700 °C, or 500 °C with a background strain rate) are required for this process to occur in a time scale of 10 Myr with rheological parameters expected for the crust

and mantle. The high temperatures required for dense lower crustal mafic-ultramafic cumulates to sink into the mantle suggests that this process is restricted to arcs, volcanic rifted margins, and continental regions that are either undergoing extension, are underlain by a mantle plume, or have had part of the conductive upper mantle removed.

Introduction

A fundamental problem in understanding the formation of continental crust is that the majority of magmas erupted on earth are basaltic, and yet the continents do not have a basaltic bulk composition. Continental crust has an average composition that can be characterised as high Mg# andesite (i.e. molar Mg# > 0.5, $SiO_2 > 55$ wt %, and less than 10 wt% MgO; see Kelemen (1995), Rudnick (1995), and references therein). High Mg# andesite lavas with major and trace element compositions similar to the continental crust are found at arcs, suggesting that continental crust formed as a result of arc magmatism (e.g. Taylor, 1967). However, of the magmas erupted at arcs, a substantial portion are basaltic (e.g. Kay and Kay, 1994), and many of the dacitic to andesitic lavas are evolved, with lower Mg#'s than the continental crust.

Fractionation of a hydrous basaltic parent magma at oxygen fugacities observed in arc magmas has not been shown by melting experiments [along a fractionation trend (e.g. "basalt" to "granite")], to produce high Mg# andesite (Kelemen, 1995). Mixing of end-member compositions, via magma mixing, assimilation, and/or in mechanical, tectonic juxtaposition, however, can produce the high Mg# andesite composition of the bulk continental crust (e.g. Grove et al., 1982; McBirney et al., 1987). For a mixing mechanism to generate bulk crust with a high Mg# andesite composition, some process is required to remove the cumulates and residues formed during generation of the silicic, "granitic" end-member (Figure 1). "Delamination" of the lower crust has been suggested as a possible mechanism for the removal of the mafic residues of basalt differentiation (Kay and Kay (1985, 1988, 1990, 1991); Arndt and Goldstein (1989); Turcotte (1989)). Kay and Kay (1991, 1993) proposed that a mafic lower crust, if it is thickened and cooled sufficiently, will convert to a high density mineral assemblage, leading to a gravitationally unstable configuration in which the lower crust can sink into the underlying lower-density mantle.

Until now there have been few efforts to quantitatively assess the dynamics of dense lower crust. Convective instability of cold, conductively cooled upper mantle beneath orogenic belts

has been the subject of a considerable amount of attention (e.g. Houseman and Molnar, 1997). In this case, crustal shortening enhances the small density contrast that has been proposed to exist between the conductively cooled and thickened conductive upper mantle and the underlying convecting mantle. However there has not yet been any attempt to quantitatively assess the consequences of a potentially much larger density contrast between the mafic/ultramafic lower crust and the conductive underlying mantle. In this paper we consider the development of convective instabilities in dense mafic and ultramafic cumulates in the lower crust. This process is distinct from "delamination" because the lower crust does not "peel off" (as proposed by Bird (1978, 1979)), but rather forms "blobs" that drip off the base of the crust. However, the result of "delamination" and "convective instability" is essentially the same thing: sinking of dense lower crust into the lower density mantle. By calculating the equilibrium subsolidus phase assemblage for a suite of lower crustal and mantle compositions, we determine the density contrast that is expected between the lower crust and underlying mantle. We then use this information, along with rheological parameters for the lower crust and mantle, to determine the time scales for the development of two-dimensional lower crustal convective instability using both a linear analysis and finite element code developed by G. A. Houseman.

In initiating this study, we reasoned that convective instability of the lower crust might be dynamically impossible. In this view, the density contrast between lower crust and conductively cooled upper mantle would be controlled primarily by temperature. At high temperature, even though the lower crust is compositionally distinct from the mantle, it might be buoyant (Kay and Kay, 1993). At low temperature, where lower crust might be denser than mantle, viscosities might be so high that a convective instability could not occur in geologically relevant times. At intermediate temperatures, we reasoned, there might be a "window" in which lower crust is denser than upper mantle and viscosities remain low enough to permit an instability to develop. We show in this study that this window of instability is wide, and that lower crustal instabilities are likely at pressures higher than 1.0 GPa, even at near solidus conditions.

Lower Crustal Compositions and SubSolidus Phase Equilibria

To become convectively unstable, the lower crust must be denser than the mantle. To determine the density contrast, we chose a number of bulk compositions that span the likely compositional range of the lower crust and mantle and calculated their densities from a subsolidus equilibrium phase assemblage program developed by Connolly (1990).

The bulk compositions that we considered for the lower crust and mantle are listed in Table 1. All lower crustal lithologies considered are “mafic”, as indicated by the majority of seismic refraction data from continental crust (e.g. Rudnick and Fountain, 1995; Christensen and Mooney, 1995; and references therein) from volcanic arcs (e.g. Gill, 1981; Suyehiro et al., 1996; Parsons et al., 1998; Holbrook et al., 1999; Fliedner and Klemperer, 1999; and references therein) and from volcanic rifted margins (e.g. White et al., 1987; Zehnder et al., 1990; Barton and White, 1997; and references therein). These include relatively refractory cumulate or restite compositions that range from a lower crustal gabbro of the Wadi Tayin Massif in the Oman ophiolite (low P gabbro), an inferred high pressure gabbro from beneath the Faeroes Islands flood basalt section (high P gabbro), a typical ultramafic cumulate xenolith from the Aleutian arc (olivine clinopyroxenite), a lower crustal average composition exposed in the Talkeetna arc section of south-central Alaska (arc gabbronorite), a median composition from a worldwide compilation of granulite xenoliths (“average” granulite), and a primary basalt composition from East Greenland (basalt). Though it is unlikely that a basalt “liquid” composition would be present in the lower crust, we include it here for comparison with the results for the cumulate compositions. The mantle was considered in terms of depleted and primitive end members, ranging from a highly depleted mantle harzburgite from the Archean craton of East Greenland (“cratonic” peridotite), through a typical composition of residual mantle peridotite dredged from the southern mid-Atlantic ridge, American-Antarctic Ridge and Southwest Indian ridge (abyssal peridotite), to an inferred primitive mantle composition

(pyrolite).

The subsolidus phase equilibria calculations were performed on initial compositions that include only the major element oxides SiO_2, Al_2O_3, FeO, MgO, CaO, and Na_2O. We excluded TiO_2, K_2O, and P_2O5 because these elements introduce uncertainty in the results and are unlikely to significantly affect the calculated subsolidus mode. Cr_2O_3 was excluded in the Connolly (1990) subsolidus code, even though it is important for the formation of spinel. We tested the effect of excluding Cr_2O_3 by suppressing garnet formation in our mantle compositions and found that density was lower by only about 10 kg/m^3. Amphibole was not included because of the complexity of the solid solutions of this mineral. However, omitting this mineral phase would favour the formation of garnet at lower pressures. Thermodynamic databases of both Holland and Powell (1998) and Berman (1996) were used in the subsolidus calculations. Except for a difference in mantle densities calculated over a large pressure range (see discussion), the difference in densities calculated using these two databases was small, and so in all results presented here we use only Holland and Powell's (1998) more recent data base.

Reaction rates for the transformation of gabbroic rocks to denser eclogite facies (i.e. garnet + omphacite) are poorly known. Hacker (1996) points out that most gabbroic rocks are transformed to eclogite at temperatures $\geq$550°C, and that examples of incomplete transformation above 800°C are rare. Therefore, to approximate finite reaction times for phase equilibrium to be attained at subsolidus conditions, we fixed the lowest temperature of phase equilibration at 800 °C. At temperatures below 800 °C, we corrected the density at constant pressure using the bulk expansivity and compressibility, but kept the equilibrium phase proportions (i.e. mode) constant.

Densities calculated for the six crustal compositions listed in Table 1 are shown in Figure 2 as a function of temperature and pressure. The effect of the imposed minimum equilibration temperature is that the density changes very little at a given pressure for temperatures less than 800 °C. The density of all compositions increases with increasing pressure as garnet becomes a stable mineral phase, with this transition occurring at higher pressures with increasing temperature. At

temperatures below 800 °C, garnet is stable at and above ∼0.8 GPa, for all compositions except olivine clinopyroxenite (Figure 2e), in which very little garnet forms because of the low aluminum content.

Performing these calculations on the three mantle compositions listed in Table 1 allowed us to determine the density contrast between the lower crustal and mantle compositions at a given temperature and pressure. The density contrast calculated by taking the difference between the crustal compositions of Figure 2 and the density of pyrolite at the same P-T conditions ($\Delta\rho = \rho_{crust} - \rho_{mantle}$) is shown in Figure 3. Comparison of the pyrolite with the crustal densities gives us a minimum bound on the expected density contrast because pyrolite is the densest mantle composition. Contours are shaded everywhere that the crustal compositions are more dense than the mantle. The results show that, at temperatures less than 800 °C, the minimum pressure at which the lower crust is denser than the mantle is ∼0.25 GPa for olivine clinopyroxenite, ∼0.8 GPa for arc gabbronorite and basalt, ∼1.5 GPa for high and low P gabbro, and ∼2 GPa for average granulite.

To determine the density contrast between the crust and mantle in different tectonic settings, we chose "hot" and "cold" end-member geotherms and then calculated the resulting density profile. We will refer to the geotherms by their temperatures at 1 GPa, which is approximately the Moho pressure in typical continental crust (Rudnick and Fountain, 1995; Christensen and Mooney, 1995), arcs (Gill, 1981; Suyehiro et al., 1996; Parsons et al., 1998; Holbrook et al., 1999; Fliedner and Klemperer, 1999), and volcanic rifted margins (White et al., 1987; Zehnder et al., 1990; Barton and White, 1997). Notable exceptions are crustal thicknesses in excess of 60 km in the Andes (e.g. Isacks, 1988) and Himalaya and Tibet (e.g. Chen and Molnar, 1981). Profiles of the calculated density and modal composition corresponding to a "cold" 300 °C Moho (surface heat flow of ∼40 mW/m^2) for four of the crustal compositions and compared to the density of pyrolite are shown in Figure 4. For all compositions, an increase in density at ∼ 0.8 GPa corresponds to the formation

of garnet according to the reaction $plagioclase + olivine = garnet$, as for example

$$\underset{\text{Anorthite}}{\mathrm{CaAl_2Si_2O_8}} + \underset{\text{Forsterite}}{\mathrm{Mg_2SiO_4}} = \underset{\text{Pyrope-Grossular Garnet}}{\mathrm{CaMg_2Al_2Si_3O_{12}}}. \quad (1)$$

Despite solid solutions in all of these phases, the "olivine-out" isograd is calculated to be sharp for all of the mafic compositions.

Throughout almost the entire P-T range, the average granulite composition is less dense than the gabbroic composition, while the olivine clinopyroxenite is denser than the mantle even without garnet present. Densities of the three gabbroic compositions in Figure 4 differ due to: (a) high Mg/Fe in the gabbro and granulite compositions compared to the arc gabbronorite, and (b) the unusually high Al_2O_3 content of the arc gabbronorite (19.26 wt%). Both of these factors lead to formation of larger quantities of garnet at lower pressures in the arc gabbronorite composition. It should be emphasised that the arc gabbronorite we have chosen is an average of 16 analyses of lower crustal samples from the Talkeetna arc section (Burns, 1983), all of which show high Al_2O_3 from 16.18 to 23.28 wt%, and is very similar to another average of lower crustal gabbronorite compositions from the Talkeetna section (Debari and Sleep, 1991) with 18.69 wt% Al_2O_3. Furthermore, this composition is remarkably similar to aluminous gabbronorite from the Kohistan arc section (Miller and Christensen, 1994). Thus, the presence of aluminous gabbronorite, with relatively low Mg/Fe compared to ophiolites and layered gabbro intrusions, is well documented for arc lower crust.

The calculated density profiles for all of the crustal and mantle compositions listed in Table 1 is shown in Figure 5 for the 300 °C "cold" geotherm. The density of cratonic peridotite is less than pyrolite by $\sim$75 kg/m^3, and the abyssal peridotite has a density similar to that of the pyrolite. When compared to the crustal compositions, the lower density of the cratonic peridotite does not change the pressure at which the crustal densities exceed that of the mantle. All compositions show an increase in density at about $\sim$0.8 GPa when garnet forms, but the amount of garnet that forms is dependent on the proportions of olivine and plagioclase in the equilibrium mineral assemblage

at low pressures.

To explore the effects of a “hot” geotherm on the density contrast between the crust and mantle, we calculated density profiles along geotherms with Moho temperatures of 800 °C and 1000 °C (Figure 6). The conductive part of these geotherms extends to the pressure at which the geotherm intersects the mantle adiabat. This transition depth is shown as a grey horizontal line in the density plots. At high temperatures, both the “high P”and “low P” gabbro compositions are less dense than the mantle over almost the entire pressure range considered. The arc gabbronorite and basalt compositions have densities that differ markedly between the 800 °C and 1000 °C geotherms. For the 800 °C geotherm, both compositions are denser than the mantle, but for the 1000 °C geotherm, both have densities that are less than that of the mantle down to the base of the conductive geotherm. The reason for this density decrease is that the P-T boundary of the garnet stability field lies between the 800 and 1000 °C geotherms for these compositions.

(Note that, in fact, the arc gabbronorite composition would be partially molten at 1300 °C and 1.2 GPa, and this effect has not been incorporated into our density calculations. As well, the time taken for phase transformations to occur would be lowered if melting occurred, and if the melt migrates upward, the density of the residues from the melting would be greater than that of the unmelted rock (Kay and Kay, 1993).)

The evolution of temperature and density for the arc gabbronorite starting from an initial 1000 °C geotherm and cooling conductively to an 800 °C geotherm is shown in Figure 7 . The depth to the base of the conductive geotherm increases from 1.2 to 1.6 GPa in this calculation. The result shows a transition from an initially stable configuration of positively buoyant arc lower crust at high temperature to a dense and unstable lower crust as a result of relatively small amounts of cooling on a time scale of $\sim$10.2 Myr.

In summary, subsolidus phase equilibria calculations show that density of mafic and ultramafic lower crustal compositions can exceed the density of the mantle, but the pressure at which this occurs is a strong function of composition and temperature. With a “cold” geotherm, relevant to

cratonic settings, the density of five of the six lower crustal compositions exceeds that of the mantle at a minimum pressure between $0.25 - 1.5$ GPa. Olivine clinopyroxenite, arc gabbronorite, and basalt have densities that are greater than that of the mantle at minimum pressures less than 1.0 GPa. The density contrast between the crust and mantle varies from 50-250 kg/m^3, depending on the compositions chosen. For a "hot" geotherm, densities are lower, with only olivine clinopyroxenite, arc gabbronorite, and basalt being denser than the mantle if the Moho temperature is 800 °C. For a 1000 °C Moho, olivine clinopyroxenite is the only composition denser than the mantle, because its density is not dependent on the formation of garnet.

Rheology of the Lower Crust and Mantle

The time scale over which a dense lower crust can become convectively unstable is not only dependent on the density contrast, but also the strength of the lower crust and mantle. To assess the effect of rheology on the development of convective instabilities, both dislocation creep and diffusion creep were considered as end member deformation mechanisms. The general form of the flow law is given by

$$\dot{\epsilon} = A\sigma^n exp(-Q/RT)d^m \tag{2}$$

where $\dot{\epsilon}$ is the strain rate, A is an empirical constant, σ is the differential stress ($\sigma_1 - \sigma_3$), Q is the activation energy, R is the universal gas constant, T is the absolute temperature, d is the grain size, and m and n are exponents that depend on the mechanism controlling deformation. For dislocation creep ($m = 0$; $n > 1$) the strain rate is independent of the grain size but varies nonlinearly with the stress, while for diffusion creep ($m < 0$; $n = 1$) the strain rate varies linearly with the stress, but nonlinearly with the grain size. In general, the transition from diffusion creep to dislocation creep occurs when the differential stress is large ($\sim$ 100 MPa for dry olivine of Hirth and Kohlstedt (1995)). In this study, we examine the effect of the end-member deformation

mechanisms separately and do not take into account the transition from diffusion to dislocation creep.

Experimentally determined rheological parameters can be related to those used for viscous flow by assuming a general constitutive relation between deviatoric stress τ_{ij} and strain rate $\dot{\epsilon}_{ij}$

$$\tau_{ij} = B\dot{E}^{1/n-1}\dot{\epsilon}_{ij} \tag{3}$$

where $\sigma_{ij} = p\delta_{ij} + \tau_{ij}$, B is a rheological coefficient, $\dot{E}$ is the second invariant of the strain rate tensor, and n is the stress exponent. The effective viscosity (η) can then be written as

$$\eta = \frac{B}{2}\dot{E}^{1/n-1}. \tag{4}$$

where the rheological coefficient, B, is a function of the rheological parameters and is defined as

$$B = A^{-1/n}\exp\left(\frac{Q}{nRT}\right). \tag{5}$$

For diffusion creep $\eta = B/2$ and the strain rate varies linearly with the applied stress. For dislocation creep, η varies nonlinearly with the the strain rate, so that increasing the strain rate decreases the effective viscosity.

The values of rheological constants relevant to the lower crust and mantle are listed in Table 2. For the mantle, it is generally agreed that olivine is the main phase controlling deformation (e.g. Hirth and Kohlstedt, 1996). For the lower crust, garnet and omphacite (sodium-rich clinopyroxene) have been proposed as the main phases controlling deformation. Experimental results on the deformation of omphacite are not available. However, the measured flow laws for diopside (clinopyroxenite) and jadeite are possible end-members. Effective viscosities of clinopyroxenite, jadeite, garnet, dry olivine, and wet olivine calculated from

$$\eta = \frac{\sigma}{\dot{\epsilon}} = \sigma^{(1-n)}A^{-1}\exp\left(\frac{Q}{RT}\right) \tag{6}$$

are shown in Figure 8 as a function of differential stress at temperatures of 600, 900 and 1200 °C. It is clear that dry olivine has the highest effective viscosity, and is significantly stronger than garnet.

Clinopyroxenite and wet olivine have similar effective viscosities, and are also generally stronger than garnet. These mineral phases have effective viscosities that span nearly 10 orders of magnitude at low temperatures, and about 5 orders of magnitude at high temperatures; it is clear that the rheological properties of the lower crust are highly variable. We therefore chose two different rheological models for the crust and mantle: one where the crust is strong and has the same stress exponent ($n = 3.5$) and rheological coefficient ($B_1/B_0 = 1$) as the underlying mantle, and another where the lower crust has the same stress exponent, but is weak and has a rheological coefficient that is two orders of magnitude less than the mantle ($B_1/B_0 = 0.01$). This choice of rheological coefficients is based on the results shown in Figure 8and the fact that, at a given differential stress, $B \propto \eta^{1/n}$. Our choice of stress exponent for the crust is based on the fact that very little difference was found between results with n ranging from 3.3 to 3.6.

Convective Instability of Dense Lower Crust

To investigate the removal of dense mafic cumulates from the base of the crust, we assume that this process occurs as a convective instability, resulting from a dense fluid overlying a less dense fluid in a gravitational field. This problem has been studied extensively (e.g. Rayleigh, 1883; Taylor, 1950; Chandresekhar, 1961; Whitehead and Luther, 1975; Canright and Morris, 1993; Houseman and Molnar, 1997). We use a linear analysis that follows the development of Conrad and Molnar (1997) and Bassi and Bonnin (1988), and the two dimensional finite element code of G. A. Houseman in order to determine growth rates and time scales of this process. Linear analysis of Rayleigh-Taylor instability allows for the solution of the equation of motion for infinitesimal deflections of the interface between the dense layer and underlying low density layer for both linear and non-linear viscosity. However, use of finite element code to characterise this process for non-Newtonian viscosity is important for accurately determining the growth of an instability at large amplitudes because the viscosity depends on the strain rate, which varies spatially (Houseman

and Molnar, 1997). We use both a linear analysis and finite element code to study the growth of convective instabilities with a linear viscosity, but use only the finite element code to study the growth of instabilities for a non-linear viscosity. The linear analysis is not presented here in detail because it is outlined extensively in Conrad and Molnar (1997), and because with multiple layers (i.e. more than 2) it is not possible to obtain simple analytic expressions.

A schematic depiction of the layout and parameters chosen for a dense lower crustal layer overlying a less dense mantle is shown in Figure 9. A neutrally buoyant upper crustal layer is included to take into account decoupling of the dense layer from the rigid surface. Since the driving force for the development of an instability is the density contrast between the dense layer and mantle ($\Delta\rho = \rho_1 - \rho_0$), densities are considered with reference to this density contrast. Based on earlier results from subsolidus phase equilibria calculations, we approximate $\Delta\rho$ for the dense layer as constant. However, because of the strong dependence of rheology on temperature, we consider the effect of allowing the viscosity of the mantle to decay exponentially with depth. Boundary conditions are set so that the upper boundary is rigid ($w = u = 0$), the sides are reflecting ($u = \sigma_{xz} = 0$), and the lower boundary of the mantle is allowed to deform as a free surface ($\sigma_{zz} = \sigma_{zx} = 0$). The upper layer is neutrally buoyant and has a rheology that is identical to that of the dense layer, so that the upper layer acts only to decouple the dense layer from the rigid surface boundary condition. The interface between the dense layer and the mantle is initially perturbed with a sinusoidal deflection with amplitude Z_0 and wavelength λ. Without this initial perturbation to the interface, an instability would not develop.

Solving the Navier-Stokes equations with inertial terms neglected (i.e. Stoke's flow) is facilitated by non-dimensionalisation. Doing so aids in determining the fundamental behaviour of the solution, and leads to the definition of characteristic scaling values for length, density, and viscosity. For length scales, we chose either the dense layer thickness h or viscous decay length L of the mantle, depending on whether the viscosity profile of the mantle is constant, or exponentially decreasing. The density contrast between the dense layer and mantle $\Delta\rho$, and the rheological co-

efficient B at the top of the mantle were chosen as the other characteristic scaling values, leading to a time scale given by

$$T = \left(\frac{B}{2\Delta\rho g[h, L]} \right)^n, \tag{7}$$

where $[h, L]$ implies that either h or L is used, depending on the whether the dense layer thickness or viscous decay length of the mantle are used. This scaling equation contains the fundamental interdependency of the various parameters which affect the time scale for the growth of an instability. In the following sections, non-dimensional (primed) quantities refer to their dimensional counterparts with the following relations:

$$Z = Z'[h, L]; \quad \lambda = \lambda'[h, L]; \quad t_b = t'_b T; \quad q = q'/T; \quad u = u'[h, L]/T; \quad \dot{\epsilon} = \dot{\epsilon}'/T \tag{8}$$

Exponential decrease in viscosity in the mantle was characterised in terms of the ratio between the length scale of viscous decay and thickness of the dense layer (L/h). Values of L/h of 3.474, 1.158, and 0.8681 were chosen in order to approximate the decrease in viscosity over 1, 5, and 10 km length scales in the conductively cooling mantle. Exponentially decreasing viscosity approximates the effect of a conductive geotherm, where the temperature changes significantly with depth over the thickness of the conductively cooled upper mantle, while a constant viscosity profile approximates the effect of an adiabat, where the temperature changes very little over the depth range considered.

The development of a convective instability caused by an initially small displacement to the base of the dense layer is shown in Figure 10a. In this finite element calculation, the initial displacement is in the form of a sinusoidal perturbation with a wavelength equal to the horizontal extent of the dense layer, but it is clear that the fastest growing wavelength is much shorter and dominates the behaviour of the instability at later times. For the fastest growing wavelength, Figure 10b shows a series of snapshots at different times during the development of an instability. Starting initially from an undeformed state, the time series shows the formation of an instability and the dense layer sinking into the underlying mantle. In this example the horizontal extent is

half the total wavelength (i.e. mirror symmetry is assumed at the edge of the layers). The initial displacement of the dense layer is greatest on the left, and it is clear that this is where the instability initiates. Note that the entire dense layer participates in the instability. Growth of the instability is determined by tracking the depth of maximum displacement of the interface as a function of time.

For a Newtonian viscosity, a convective instability grows exponentially with a growth rate q', starting from an initial displacement Z'_0 according to

$$Z' = Z'_0 \exp(q't'). \tag{9}$$

The maximum downward displacement of the instability (Z') as a function of time (t') is shown in Figure 11a. Also shown is the result of plotting $ln(Z')$ as a function of time, which yields a nearly straight line and indicates that the growth is exponential. It is convenient to define the instability time t'_b for a Newtonian viscosity as the time at which the interface is displaced downwards by an amount equal to the initial dense layer thickness

$$t_b = -\frac{1}{q'} \ln \left(\frac{Z'_0}{Z'} \right) T. \tag{10}$$

For non-Newtonian viscosity, the dependence of viscosity on strain rate causes fundamentally different behavior in the growth of an instability. Growth is super-exponential, but is initially slow at small deflections of the interface. With time, growth rates increase as the the deflection of the interface increases, leading to the rapid and almost instantaneous deflection of the interface (Figure 11b). Houseman and Molnar (1997) derived a simplified theory that approximates this behaviour, where the vertical displacement of the boundary is given by

$$Z' = \left[(n-1) \left(\frac{C'}{n} \right) (t'_b - t') \right]^{\frac{1}{1-n}} \tag{11}$$

and the instability time is given by

$$t_b = \left(\frac{n}{C'} \right)^n \frac{Z_0'^{(1-n)}}{(n-1)} T \tag{12}$$

where C' is a growth rate factor and is analogous to q'. Plotting $Z'^{(1-n)}$ as a function of time yields a linear relationship (Figure 11b), verifying that that deflection increases according to equation (11), and allows calculation of the growth rate C'. The abrupt initiation and completion of the instability for non-Newtonian rheologies occurs at a small fraction of the initial displacement.

Newtonian Viscosity (Diffusion Creep)

Growth rates for a Newtonian viscosity calculated from both a linear analysis and finite element experiments are shown as a function of wavenumber in Figure 12. The results show that the finite element calculations (points) are consistent with the linear analysis (curves). Determining the fastest growing wavelength of the instability is important for characterising the instability, since this wavelength will eventually dominate the growth, regardless of the wavelength of the initial perturbation. In Figure 12a the dense lower crustal layer is strong and has a rheological coefficient equal to that of the mantle ($B_1/B_0 = 1$) and in Figure 12b the dense lower crustal layer is weak and has a rheological coefficient that is two orders of magnitude less than that at the top of the mantle ($B_1/B_0 = 0.01$). The effect of exponentially decreasing B_0 in the mantle with depth ($L/h = 3.474, 0.8681$) is also shown and compared to a case where B_0 is constant ($L >> h$). For a strong dense layer, maximum (non-dimensional) growth rates (q'_{max}) are ~0.15 – 0.25, while for a weak dense layer maximum growth rates are ~4 – 12, depending on the decay length of B_0 in the mantle. The wavenumber of maximum growth rate (k'_{max}) is about 0.9 for a strong dense layer and 0.5 for a weak dense layer, corresponding to wavelengths of 7 and 12.5 times the dense layer thickness, respectively. Limiting values of maximum growth rate (q'_{max}) and wavenumber (k'_{max}) as a function of L/h calculated from the linear analysis are shown in Figure 13. It is clear that the wavenumber of fastest growth reaches values of 0.9 and 0.3 (for strong and weak dense layers, respectively) when there is a constant rheological coefficient in the mantle $L >> h$, and 1.1 and 1.5

when there is a strongly depth dependent rheological coefficient ($L << h$). These results show that the rheological coefficient of the dense layer and the decay length of rheological coefficient in the mantle can strongly influence the growth rate of the instability. Furthermore, combining a weak dense layer with a strongly depth dependent mantle rheological coefficient produces the fastest growth rates: the weak dense layer experiences very little viscous resistance from the mantle as the decay length (L/h) in the mantle decreases.

To determine dimensional instability times from the maximum growth rates shown in Figure 12, we scale the results using equations (7) and (10). For the fastest growing wavenumber, Figure 14 shows the calculated instability time as a function of Moho temperature for 1 and 10 km thick strong and weak dense lower crustal layers, and density contrasts of 50, 100, and 200 kg/m^3. The Moho temperature required for a 10 Myr instability is shown by the vertical shaded bars, and is related to the rheological coefficient at the top of the mantle by equation (5). For a 10 km thick, strong dense layer (Figure 14a), a 950-1000 $^\circ$C Moho temperature is required for an instability to develop with a density contrast of 50-200 kg/m^3 and a constant rheological coefficient mantle. A 1 km thick dense layer requires Moho temperatures about 100 $^\circ$C greater for the same instability time. It is clear that the density contrast has a smaller effect on the instability time than the rheological coefficient (i.e. Moho temperature) because the rheological coefficient varies by orders of magnitude over the temperature range considered, but the density contrast varies by less than one order of magnitude. An exponentially decreasing rheological coefficient for the mantle decreases the required Moho temperature for an instability to develop by an almost insignificant amount (Figure 14c), indicating that the strength of the dense layer is important in controlling the time scale for the formation of a convective instability. For a weak dense layer overlying a constant rheological coefficient mantle (Figure 14b) convective instability of the dense layer occurs in 10 Myr if the Moho temperature is about 900 $^\circ$C for a 10 km thick dense layer and 1000 $^\circ$C for a 1 km thick dense layer. The lowest Moho temperature for a 10 Myr instability occurs with an exponential decaying rheological coefficient in the mantle and a dense layer that is weak (Figure 14d).

Moho temperatures in this case are ∼800 °C for an instability time of 10 Myr for a 10 km thick dense layer, and ∼950 °C for a 1 km thick dense layer. These instability times refer to an initial displacement of $Z_0 = 1\%$. A larger initial displacement does not change the exponential growth rate of the instability.

Non-Newtonian Viscosity (Dislocation Creep)

The growth rate factor (C') for a non-Newtonian viscosity with $n = 3.5$ for all layers is shown in Figure 15. An additional decay length for the rheological coefficient of the mantle was included in these results ($L/h = 1.1581$) in order to help clarify the dependence of growth rate factor on the decay length of B_0, because an accurate linear analysis cannot be made. When the dense lower crustal layer is strong ($B_1/B_0 = 1$) the wavenumber of fastest growth is about $k'_{max} = 1.5$, and when the dense lower crustal layer is weak ($B_1/B_0 = 0.01$) the fastest growing wavenumber is about $k'_{max} = 0.5$. Compared to the results for a Newtonian viscosity, k'_{max} is shifted to slightly higher values, and corresponds to wavenumbers of maximum growth rate factor of ∼4.2 and 12.5 times the dense layer thickness, respectively. It is also clear from the results that the growth rate factor (C') depends only weakly on L for $L/h < 1.158$.

Instability times for the fastest growing wavenumbers for strong and weak dense layers are shown in Figure 16. These results all assume an initial perturbation of the interface between the dense layer and the mantle of 100 % of the initial dense layer thickness. Houseman and Molnar (1997) showed that for non-Newtonian viscosity, the instability time for an instability with different initial deflections is related by

$$t'_{b_1} = t'_{b_2} \left(\frac{Z'_{0_1}}{Z'_{0_2}} \right)^{1-n} \tag{13}$$

Therefore, changing the initial deflection of the boundary from 100% to 1% of the initial dense layer thickness will increase the instability time by a factor of 10^5. The change in Moho tempera-

ture for an instability to develop on the same time scale can then be calculated from

$$\frac{1}{T_{Moho_1}} - \frac{1}{T_{Moho_2}} = \frac{nR}{Q} \ln \left(\left[\frac{t_{b_1}}{t_{b_2}} \right]^{1/n} \right) \tag{14}$$

and is about 150 °C if the Moho is 600 °C, and about 350 °C if the Moho is 1000 °C.

For a strong dense layer overlying a constant rheological coefficient mantle (Figure 16a), the Moho temperature required for an instability to develop in 10 Myr is ∼900-1000 °C for a 10 km thick dense layer, and ∼1100-1300 °C for a 1 km thick dense layer, depending on the density contrast. Note that since the instability time depends in part on $\Delta\rho^{-3.5}$, the effect of the density contrast on Moho temperature is larger for a non-Newtonian viscosity than for a Newtonian viscosity where the instability time depends on $\Delta\rho^{-1}$. An exponentially decreasing rheological coefficient in the mantle requires Moho temperatures about $\sim$ 50 °C less than if the rheological coefficient is constant. A weak dense layer over a constant B_0 mantle requires a Moho temperature of ∼800-900 °C for a 10 km thick dense layer, and ∼1000-1150 °C for a 1 km thick dense layer to become unstable in 10 Myr (Figure 16b). As with a Newtonian viscosity, an exponentially decreasing B_0 in the mantle and a weak dense layer results in the lowest Moho temperatures. These are ∼650-700 °C for a 10 km thick dense layer and ∼900-1000 °C for a 1 km thick dense layer to become unstable in 10 Myr. For "wet" olivine, the rheological coefficient is about one order of magnitude less (see Figure 8), resulting in a decrease in Moho temperatures of 100-150 °C for an instability to develop in 10 Myr.

Horizontal Shortening and Non-Newtonian Viscosity

Imposing an initial background strain rate when the viscosity is non-Newtonian reduces the initial effective viscosity, and therefore decreases the instability time. Molnar et al. (1998) show that the deformation can be divided into two separate stages: an initial period of exponential growth followed by a period of super-exponential growth. The growth rate for the initial stage is determined by the effective viscosity caused by the initial background strain rate. To quantify this effect

for the dense lower crustal layer, we performed numerical experiments with different initial horizontal strain rates. Figure 17 shows the instability time (t'_b) as a function of horizontal strain rate ($\dot{\epsilon}'_{xx}$) for strong and weak lower crust. After $\dot{\epsilon}'_{xx}$ exceeds a threshold value, the instability time decreases in proportion to the increase in strain rate (as viewed on a log-log plot). Higher initial horizontal strain rates cause shorter instability times because of lower initial effective viscosities. In practice it it is difficult to explore this effect numerically because large initial horizontal strain rates change the dimensions of the dense lower crustal layer, leading to a change in the wavelength of the instability. For the results shown in Figure 17, the maximum horizontal strain rate in our numerical experiments reduces the horizontal dimension of the dense layer by about 20%, but this does not affect our estimates of maximum growth rate factor significantly.

We can exploit the linear relationship between instability time and horizontal strain rate (shown in Figure 17) to determine the change in instability time for larger strain rates, assuming that this linear relationship still holds. The change in instability time for a given initial horizontal strain rate, after simplification, is given by

$$t_{b'} = \begin{cases} t'_{b0} \left(\frac{\dot{\epsilon}'_{xx}}{\dot{\epsilon}'_{xx_0}} \right)^{-\frac{\dot{\epsilon}'_{xx}}{t_{b'}} \frac{dt'_b}{d\dot{\epsilon}'_{xx}}} & \dot{\epsilon}'_{xx} \geq \dot{\epsilon}'_{xx_0} \\ t'_{b0} & \dot{\epsilon}'_{xx} < \dot{\epsilon}'_{xx_0} \end{cases} \tag{15}$$

where t'_{b_0} is the non-dimensional instability time with no initial horizontal strain rate, $\dot{\epsilon}'_{xx_0}$ is the minimum initial strain rate at which the instability time is affected by horizontal shortening, and $dt'_b/\dot{\epsilon}'_{xx}$ is determined from Figure 17.

The effect of imposing initial horizontal strain rates of 10^{-18} s^{-1} and 10^{-14} s^{-1} on the growth of an instability with a non-Newtonian viscosity is shown in Figure 18. It is clear from the results that an initial strain rate can significantly reduce the Moho temperature required for an instability to develop. At high Moho temperatures, where instabilities develop quickly in response to the already small B_0 values, instability times are relatively unchanged by the presence of an initial background strain rate. With a strain rate of 10^{-14} s^{-1}, Moho temperatures for a 10 Myr convective instability

of 1 km thick dense layer are reduced to as low as 700-800 °C for a strong dense layer and 650-750 °C for a weak dense layer. For a 10 km thick dense layer, the same initial horizontal strain rate reduces Moho temperatures to 600-650 °C for a strong dense layer, and to 550-600 °C for a weak dense layer.

In summary, application of the scaling laws show that for a Newtonian viscosity, Moho temperatures must be greater than ∼900 °C to produce an instability in 10 Myr if we assume that 10 km is representative of the thickness of the dense lower crustal layer. Instability at temperatures as low as 800 °C is possible only if the dense lower crustal layer is weak and the decay length of the rheological coefficient of the mantle is small. Non-Newtonian viscosity requires Moho temperatures of 850-1000 °C for a 10 Myr instability, and results show a much stronger dependency on the density contrast between the dense layer and mantle than for a Newtonian viscosity. Temperatures as low as ∼700 °C can result in a 10 Myr instability if the dense layer is weak and the rheological coefficient of the mantle decays exponentially. Horizontal shortening can reduce the Moho temperature for a 10 Myr instability with a non-Newtonian viscosity to about 550-650 °C for an initial strain rate of 10^{-14} s^{-1}, assuming a dense layer thickness of 10 km. A wet olivine rheology would reduce Moho temperatures required for a 10 Myr instability by an additional 100-150 °C, because of the lower effective viscosity of $\mathrm{H_2O}$-rich olivine (Hirth and Kohlstedt, 1996).

Discussion

Calculations of subsolidus phase equilibria and convective instability times show, for likely rheologies for the lower crust and mantle, that dense mafic and ultramafic cumulates in the lower crust can initiate convective instabilities on geologic time scales. The low viscosity necessary for the development of an instability on a time scale of 10 Myr or less requires either high temperatures (>700 °C), or large initial strain rates ($\dot{\epsilon}_{xx_0} > 10^{-14} s^{-1}$). This suggests that lower crustal convective instability can be ruled out in old, tectonically stable cratonic settings where the geotherm is

cold ($\sim$300 °C at 1 GPa), and is restricted to regions where Moho temperatures are in excess of about 500 °C or, in the absence of a background strain rate, higher than about 700 °C. Thus, arcs, (young) passive margins, and continental regions in which the thermal boundary layer is thinned are likely settings for lower crustal convective instability. Large strain rates from continental extension (rifting) or shortening (orogenic zones) may help instabilities develop with colder geotherms.

In arc settings, the combined effect of high Moho temperatures (800-900 °C at 1.1 GPa) (e.g., Debari et al., 1987; Debari and Coleman, 1989) and decreased effective viscosities for wet olivine enhances the likelihood of lower crustal convective instability. Futhermore, the effects of arc magma composition favor the formation of dense lower crust. As noted by many workers (e.g., Kay and Kay, 1994), high H_2O contents in primitive arc basalts will generally suppress plagioclase stability, leading to crystallisation of abundant olivine clinopyroxenite cumulates. This, in turn, produces high-Al, derivative liquids which produce Al-rich cumulate gabbros and gabbronorites at lower pressures (e.g. Debari and Coleman, 1989). Thus the dense lower crustal compositions used in our Figures 2(e,f), 3(e,f), 4(a-d), 5(b), and 6(b) are taken from arc xenoliths (Conrad and Kay, 1984) and the base of an exposed arc crustal section in Alaska (Burns, 1993; Debari and Coleman, 1989) and may be typical of lower crustal rocks in arcs since they are similar to deep crustal rocks in the Kohistan arc section in Pakistan (Jan and Howie, 1981; Miller and Christensen, 1994).

As previously suggested by Arndt and Goldstein (1989), olivine clinopyroxenites at depths greater than about 8 km are denser than the mantle by about 50 kg/m^3 because cumulate ultramafic rocks have higher Fe/Mg than residual mantle. Along a “steady state” arc geotherm they would probably have to reach thicknesses of up to 10 km to become convectively unstable on geological time scales. However, if Moho temperatures are higher - for example if Moho temperatures are similar to liquidus temperatures for hydrous basaltic magmas, at around 1200 °C, then ultramafic cumulate layers a few hundred meters thick will become unstable in very short times, perhaps as quickly as they form, for Moho pressures of 1.0 GPa or more.

Arc gabbronorite compositions, on the other hand, have density contrasts of up to 150 kg/m^3

for 800 °C geotherms, and are less dense than the mantle at higher temperatures (i.e. 1000 °C at 1.0 GPa). Therefore arc gabbronorite lower crustal sections could initially form a stable lower crust and then become convectively unstable after garnet formation due to a small amount of cooling. Because they become dense at temperatures as high as 950 °C (see Figure 7), the low viscosities of the mantle required for short instability times will be present. Their high densities would probably cause these garnet-rich lithologies to become convectively unstable at thicknesses less than 10 km.

For continental regions, gabbro and olivine clinopyroxenite compositions are likely to represent the mafic and ultramafic component of the lower crust. Results from Figure 5 show that the gabbros and granulite xenolith compositions are generally stable at the high temperatures neeeded for convective instability, except if a composition similar to our high pressure cumulate extends to depths greater than about 40 km (1.4 GPa), in which case it will be denser by about 50 kg/m^3 with respect to our most depleted mantle composition. The olivine clinopyroxenite, on the other hand, is denser than the mantle by about 50 kg/m^3 at depths as shallow as 8 km (0.25 GPa). Thus, convective instability of ultramafic lower crustal cumulates is possible, but only if temperatures are hot due to rifting, the influence of a mantle plume, or thinning of the thermal boundary layer. Rifting will lower the effective viscosity by imposing a background strain rate on the crust and mantle as well as increasing the temperature by thinning the conductive upper mantle. In addition, the influence of a mantle plume could raise Moho temperatures significantly by increasing temperatures, by convective "erosion" of the conductively cooled upper mantle, and by advective heat transport due to both (a) ascent of melt into the crust, and (b) the ascent of isotherms during thinning of the conductive upper mantle. A further possibility is that thickened continental crust could have a hotter geotherm due to increased heating from radiogenic elements (e.g. Le Pichon et al., 1997).

In cold continental regions, convective instability of the lower crust may be possible if the conductively cooled upper mantle becomes convectively unstable first. Convective instability of the upper mantle has been proposed as a process which might account for the observation that com-

pressional thickening precedes extensional collapse of many orogens (e.g. England and Houseman, 1989; Houseman and Molnar, 1997; Molnar et al., 1998). The combined effect of decreased effective viscosities due to horizontal shortening and entrainment of the lower crust with a convectively downwelling upper mantle may cause dense lower crust to participate in "mantle" convective downwelling, as suggested by Kay and Kay (1993, 1994). If only a portion of the conductive upper mantle is convectively removed due to increased viscosities at shallow levels (Molnar et al. 1998) then the remaining thinner conductive upper mantle would have a higher temperature, potentially allowing dense lower crustal cumulates to subsequently become unstable on geologic time scales short compared with the time scale of orogeny.

The subsolidus equilibria results show that the density contrast between lower crustal and mantle compositions is likely to exceed any density contrast expected for the mantle due to conductive cooling. Controversy exists as to whether the possible density inversion caused by conductive cooling in the mantle is counterbalanced by positive compositional buoyancy of the upper mantle caused by the extraction of melt (Oxburgh and Parmentier, 1977; Jordan, 1988). In addition, we calculated the density profile for the three mantle compositions down to a depth of 200 km and found that for a conductive geotherm representative of a cratonic setting (300 °C Moho temperature), densities increased with depth when using Holland and Powell's (1998) database, but decreased with depth using Berman's (1996) database (Figure 19), because the values for the thermal expansivity and compressibility differ. This result shows that the association of a conductive geotherm with increasing density at decreasing depth in a constant composition mantle is not necessarily correct. Furthermore, since this does not take into account possible increased chemical buoyancy of the mantle at shallower depths (i.e. Jordan, 1988), the results using Holland and Powell's (1998) database suggests a stable density structure for much of the conductive continental upper mantle.

A remaining question is, what happens to dense lower crust after it becomes convectively unstable ? Does it sink into the convecting mantle or does it remain trapped in the conductively

cooled upper mantle? Our calculations do not take into account changes in density and temperature of the dense lower crustal layer after an instability is initiated. Competing effects of increasing temperature and pressure would likely change the density of a descending "blob". But from the results shown in Figure 3, the P-T trajectory of a descending lower crustal "blob" is likely to maintain the negative buoyancy contrast with the mantle. The depth to which descending blobs sink is likely to depend on the scale at which the instability forms, and whether melting occurs. It has been suggested that subducting oceanic crust, after converting to eclogite (i.e. garnet and omphacite), can sink as far as the core-mantle boundary (e.g. Van der Hilst, 1996).

In light of our results, it is interesting to speculate on the influence that lower crustal convective instability has on the thickness of continental crust, which ranges between 25 to 45 km away from orogenic belts (Holbrook et al., 1992; Rudnick and Fountain, 1995). The results of the phase equilibrium calculations show a broad P-T range in which plagioclase co-exists with garnet for all except the ultramafic composition. If the Moho transition, which is defined by an increase in P-wave velocities from approximately 7.2 km/s to 8.0 km/s, is due to the gabbro to eclogite transition it should be gradual. However seismic data indicate that for a large majority of cases, the Moho transition is sharp, and extends over only a few kilometers. Therefore the Moho is not due to a phase change, but is more likely a break between mafic crustal compositions and underlying ultramafic mantle. We can then ask, if the Moho depth is not simply the result of a pressure sensitive phase transition from gabbro to eclogite, why does the thickness of the crust vary only between 25 and 40 km worldwide? One explanation is that for isostatically compensated crust, erosion rates at the surface are highest for thick crust, thus acting to reduce the total variation in crustal thickness. Another is that lateral flow in ductile lower crust could work to decrease lateral thickness variations. However the results of this study offer an alternative, and perhaps complementary explanation. At temperatures of 800 °C or less, all the gabbro and gabbronorite compositions are denser than the underlying mantle at pressures greater than 1.0 to 1.5 GPa ($\sim$30-45 km). Though thicker crust clearly can form in collisional belts, it would seem that on timescales

of 100-1000 Myr, crustal thickness is likely determined by the density contrast between gabbro and peridotite. Further, the fact that average lower crustal granulite xenoliths are the least dense composition we considered (Figures 2 and 3) suggests that density sorting may have affected the composition of the remaining lower crust.

During igneous crustal formation, in arcs, along volcanic rifted margins, and probably beneath oceanic plateaus, Moho temperatures could conceivably be very high, close to basalt liquidus temperatures of 1200 to 1300 °C. Under these circumstances, several of the compositions we considered would be buoyant at pressures exceeding 1.5 GPa. The absence of thick crust in a number of arc settings, such as the Aleutian (Holbrook et al., 1999; Fliedner and Klemperer, 1999), Izu-Bonin (Suyehiro et al., 1996), and Cascadia arcs (Parsons et al., 1998), and along ancient volcanic rifted margins suggest that, even in Mesozoic and Cenozoic settings, crustal thickness may often be determined by density instabilities. This, in turn, implies that (a) steady state Moho temperatures are less than 1200 °C in most arcs, and (b) crustal thickness along rifted margins may have been modified by convective instability during cooling.

Conclusions

Lower crust that ranges from mafic and ultramafic cumulates to primary liquid compositions can be significantly denser than the mantle, but the density contrast is a strong function of composition, temperature, and pressure. For basaltic and gabbroic compositions, garnet must be a stable mineral phase in order for the density to exceed that of the mantle. As a result, these compositions have densities that are pressure dependent and kinetically unfavorable at high temperatures and H_2O-free conditions. In contrast, ultramafic cumulates are denser than the mantle mainly because of their composition, and not phase transformations.

For a “cold” geotherm, relevant to cratonic settings, densities of all lower crustal compositions we considered, except that of “average” granulite, exceed that of the underlying mantle by 50–

250 kg/m^3 at minimum pressures $<$1.5 GPa. Arc gabbronorite and olivine clinopyroxenite are denser than the mantle at pressures as low as 0.25-0.8 GPa. For a "hot" geotherm, relevant to arc settings and regions of crustal extension, the density of the lower crust is much more variable and the maximum density contrast ranges from $\sim$25–100 kg/m^3. Two of the gabbro compositions we considered ("high P " and "low P " gabbro) are less dense than the mantle. Arc gabbronorite and basalt have densities that a very sensitive to the temperature of the geotherm in the range of 800-1000 °C at 1 GPa. For an 800 °C geotherm, these compositions are denser than the mantle over a pressure range that is similar to that for a "cold" geotherm. But with a 1000 °C geotherm, these compositions have densities that are less than the mantle density at pressures down to the base of the conductive geotherm. Calculations of the time required for cooling of a 1000 °C geotherm to an 800 °C geotherm indicates that about 10 Myr is required for cooling, allowing the low density assemblage to convert to their high density form. Olivine clinopyroxenite has a density contrast that is nearly unchanged from the "cold" geotherm.

Calculation of the instability times for a dense, lower crustal layer to sink into the mantle show that high temperatures (greater than 700 °C, or 500 °C with an initial background strain rate) are required for this process to occur in $\sim$10 Myr. The high temperatures required for lower crustal convective instability of dense mafic-ultramafic compositions suggests that this process is restricted to arcs, volcanic rifted margins, and continental regions that are either undergoing extension, are underlain by a mantle plume, or have had part of the conductive upper mantle removed. At arcs, lower crustal convective instability of olivine clinopyroxenites and arc gabbronorite compositions can occur readily. The high densities of arc gabbronorite compositions are sensitive to small changes in temperature. This suggests that these compositions may initially form a stable lower crust at high temperatures, to be followed by subsequent cooling and densification of gabbronorite present at $>$ 1.0 GPa, leading to convective instability at Moho temperatures that are hot enough to permit short instability times. In continental regions, gabbroic compositions have densities that are generally less than the mantle at temperatures hot enough for convective instability. But, if signif-

icant quantities of ultramafic cumulates are present, it is likely that these components of the lower crust will become convectively unstable on short timescales during rifting, convective thinning of the conductively cooled upper mantle, or heating of thickened crust by radioactive decay.

Acknowledgements

The authors would like to thank Greg Houseman, Peter Molnar, and Jamie Connolly for generously sharing their programs and advice, and Othmar Muenthener, Clint Conrad, Karen Hanghoj, Greg Hirth, Jorg Renner, and Marc Hirschmann for helpful discussions. Helpful reviews by Peter Molnar, Sue Kay, and David Bercovici greatly improved this manuscript. This work was supported by an NSERC-WHOI postdoctoral fellowship to M. Jull and by NSF Research GRANT OCE XXX to Kelemen.

References

Arndt, N.T., S.L. Goldstein, An open boundary between lower continental crust and mantle; its role in crust formation and crustal recycling, *Tectonophysics,* 161, 201-212, 1989.

Barton, A. J., White, R. S., Crustal structure of Edoras Bank continental margin and mantle thermal anomalies beneath the North Atlantic, *J. Geophys. Res.*, 102, 3109–3129, 1997.

Berman, R. G., L.Y. Aranovich, Optimized standard state and solution properties of minerals; I, Model calibration for olivine, orthopyroxene, cordierite, garnet, and ilmenite in the system FeO-MgO-CaO-Al_2O_3-TiO_2-SiO_2, *Contrib. Mineral. Petrol.*, 126, 1–24, 1996.

Bernstein, S., High pressure fractionation in rift-related basaltic magmatism: Faeroe plateau basalts. *Geology*, 22, 815–818, 1994.

Bernstein, S., P. B. Kelemen, and C. K. Brooks, Depleted spinel harzburgite xenoliths in tertiary dykes from east Greenland: restites from high degree melting, *Earth Planet. Sci. Lett.*, 154, 221–235, 1998.

Bird, P., Initiation of intracontinental subduction in the Himalaya, *J. Geophys. Res.*, 83, 4975–4987, 1978.

Bird, P., Continental delamination and the Colorado plateau, *J. Geophys. Res.*, 84, 7561–7571, 1979.

Boland, J. N., T.E. Tullis, Deformation behavior of wet and dry clinopyroxenite in the brittle to ductile transition region, in *Mineral and rock deformation; laboratory studies; the Paterson volume*, edited by B. E. Hobbs, and H. C. Heard, pp. 35–49, Geophys. Mon., Washington, D. C., 1986.

Burns, L. E. The border ranges ultramafic and mafic complexes: plutonic cores of an intraoceanic island arc, Ph.D. thesis, Stanford University, 1983.

Canright, D. and S. Morris, Buoyan instability of a viscous film over a passive fluid, *J. Fluid. Mech.*, 255, 349–372, 1993.

Chandrasekhar, S., Hydrodynamic and Hydromagnetic Instability, Oxford University Press, 1961.

Chen, W. P., and P. Molnar, Constraints on the seismic wave velocity structure beneath the Tibetan plateau and their tectonic implications, *J. Geophys. Res.*, 86, 5937–5962, 1981.

Christensen, Nikolas I., Mooney, Walter D., Seismic velocity structure and composition of the continental crust; a global view, *J. Geophys. Res.*, 100, 9761–9788, 1995.

Connolly, J.A.D., Multivariable phase diagrams: an algorithm based on generalised thermodynamics, *Am. J. Sci.*, 290, 666–718, 1990.

Conrad, C. P., and P. Molnar, The growth of Rayleigh-Taylor-type instabilities in the lithosphere for various rheological and density structures, *Geophys. J. Int.*, 129, 95–112, 1997.

Conrad, W., and R. W. Kay, Ultramafic and mafic inclusions from Adak Island: crystallisation history, and implications for the nature of primary magmas and crustal evolution in the Aleutian arc, *J. Petrol.*, 25, 88–125, 1984.

Debari, S.M., S. Mahlburg Kay, and R. W. Kay, Ultramafic xenoliths from Adagdak Volcano, Adak, Aleutian Islands, Alaska: deformed igneous cumulates from the Moho of an island arc, *J. Geol.*, 95, 329–341, 1987.

Debari, S.M., and R.G. Coleman, Examination of the deep levels of an island arc; evidence from the Tonsina ultramafic-mafic assemblage, Tonsina, AlaskaPage, *J. Geophys. Res.*, 94, 4373–4391, 1989.

DeBari, S. M., N. H. Sleep, High-Mg, low-Al bulk composition of the Talkeetna island arc, Alaska: implications for primary magmas and the nature of arc crust, *Geol. Soc. of Am. Bull.*, 103, 37–47, 1991.

Dick, H. J. B., Abyssal peridotites, very slow spreading ridges and ocean ridge magmatism, in *Magmatism in the ocean basins*, edited by A. D. Saunders, and M. J. Norry, pp. 71–105, Geol. Soc., London, 1989.

England, P.C., and G.A. Houseman, Extension during continental convergence, with application to

the Tibetan Plateau, *J. Geophys. Res.*, 94, 17561–17579.

Fliedner, M., and S. L. Klemperer, Structure of an island arc: wide-angle seismic studies in the eastern Aleutian Islands, Alaska, *J. Geophys. Res.*, 104, 10667–10694, 1999.

Fram, M. S., and C. E. Lesher, Generation and polybaric differentiation of East Greenland early Tertiary flood basalts, *J. Petrol.*, 38, 231–275, 1997.

Gill, J., Orogenic andesites and plate tectonics, Springer-Verlag, New York, 1981

Grove, T. L., Gerlach, D. C., Sando, T. W., Origin of calc-alkaline series lavas at Medicine Lake Volcano by fractionation, assimilation and mixing, *Contrib. Mineral. Petrol.*, 80,160–182, 1982.

Hacker, B. R., Eclogite formation and the rheology, buoyancy, seismicity, and H20 content of oceanic crust, in *Subduction top to Bottom*, eds. G. E. Bebout, D. Scholl, S. Kirby, and J. Platt, AGU monograph 96, pp. 337–346, 1996.

Hirth, G., and D. Kohlstedt, Water in the oceanic upper mantle: implications for rheology, melt extraction and the evolution of the lithosphere, *Earth Planet. Sci. Lett.*, 144, 93–108, 1996.

Holbrook, W. S., W. D. Mooney, and N. I. Christensen, The seismic velocity structure of the deep continental crust, in *The continental Lower Crust*, edited by D. M. Fountain, R. J. Arculus, and R. W. Kay, pp. 1–44, Elsevier Sci., New York, 1992.

Holbrook, W.S., D. Lizarralde, S. McGeary, N. Bangs, and J. Diebold, Structure and composition of the Aleutian island arc and implications for continental crustal growth, *Geology*, 27, 31–34, 1999.

Holland, T. J. B., and R. Powell, An internally consistent thermodynamic data set for phases of petrological interest, *J. Metamorph. Geol.*, 16, 309–343, 1998.

Houseman, G. A., and P. Molnar, Gravitational (Rayleigh-Taylor) instability of a layer with non-linear viscosity and convective thinning of continental lithosphere, *Geophys. J. Int.*, 128, 125–150, 1997.

Isacks, B. Uplift of the Central Andean Plateau and the bending of the Bolivian Orocline, *J. Geophys. Res.*, 93, 3211–3231, 1988.

Jan, M. Q., and R. A. Howie, Petrology of minor olivine gabbros and ultramafic rocks from upper Swat, N.W. Pakistan, *Geol. Bull. Punjab Univ.*, 16, 1–10, 1981.

Ji, S., and J. Martignole, Ductility of garnet as an indicator of extremely high temperature deformation, *J. Struct. Geol.*, 16, 985–996, 1994.

Jordan, T. H., Structure and formation of the continental tectosphere, *J. Petrol.*, 1988, 11–37, 1988.

Kay, S. M., and R. W. Kay, Role of crystal cumulates and the oceanic crust in the formation of the lower crust of the Aleutian Arc, *Geology*, 13, 461–464, 1985.

Kay, R. W., and M. S. Kay, Crustal recycling and the Aleutian Arc *Geochim. Cosmochim. Acta*, 52, 1351–1359, 1988.

Kay, R. W., and S. M. Kay, Basaltic composition xenoliths and the formation, modification and preservation of lower crust, in *Exposed cross-sections of the continental crust: proceedings*, edited by M. H. Salisbury, and D. M. Fountain, pp. 401–420, Reidel, Boston, 1990.

Kay, R. W., Kay, S. Mahlburg, Creation and destruction of lower continental crust, *Geol. Rundsch.* , 80, 259–278, 1991.

Kay, R. W., Kay, S. Mahlburg, Delamination and delamination magmatism, *Tectonophysics*, 219, 177–189, 1993.

Kay, S. M. , and R. W. Kay, Aleutian magmas in space and time, in *The geology of North America*, edited by G. Plafker, and H. C. Berg, pp. 687–722, Geol. Soc. Am., Boulder, Col., 1994.

Kay, S., B. Coira, and J. Viramonte, Young mafic back arc volcanic rocks as indicators of continental lithospheric delamination beneath the Argentine Puna plateau, central Andes, *J. Geophys. Res.*, 99, 24323–24339, 1994.

Kelemen, P. B., Genesis of high Mg# andesites and the continental crust, *Contrib. Mineral. Petrol.*, 120, 1–19. 1995.

McBirney, A. R., H. P. Taylor, and R. L. Armstrong, R. L., Paricutin re-examined: a classic example of crustal assimilation in calc-alkaline magma, *Contrib. Mineral. Petrol.*, 95, 4–20, 1987.

Miller, D. J., and N. I. Christensen, Seismic signature and geochemistry of an island arc: a multidisciplinary study of the Kohistan accreted terrain, northern Pakistan, *J. Geophys. Res.*, 99, 11623–11642, 1994.

Molnar, P., G. A. Houseman, and C. Conrad, Rayleigh-Taylor instability and convective thinning of mechanically thickened lithosphere: effects of non-linear viscosity decreasing exponentially with depth and of horizontal shortening of the layer, *Geophys. J. Int.*, 133, 568–584, 1998.

Oxburgh, E. R., and E. M. Parmentier, Compositional and density stratification in oceanic lithosphere: causes and consequences, *J. Geol. Soc. London*, 133, 343–355, 1977.

Pallister, J. S., Parent magmas of the Semail ophiolite, Oman, in *Ophiolites and oceanic lithosphere*, edited by I. G. Gass, S. J. Lippard, and A. W. Shelton, pp. 63–70, Geol. Soc., London, 1984.

Parsons, T., Trehu, A. M., Luetgert, J. H., Miller, K. C., Kilbride, F., Wells, R. E., Fisher, M. A., Flueh, E. R., ten Brink, U. S., Christensen, N. I., A new view into the Cascadia subduction zone and volcanic arc; implications for earthquake hazards along the Washington margin, *Geology*, 26, 199–202, 1998.

Rayleigh, Lord, Investigation of the character of an incompressible heavy fluid of variable density, *Proc. Lond. Math. Soc.*, 14, 170-197.

Ringwood, A. E., Composition and origin of the Earth, in *The Earth: its origin, structure and evolution*, edited by M. W. McElhinny, pp. 1–54, Acad. Press., London, 1979.

Rudnick, R. L., Making continental crust, *Nature*, 378, 571–578, 1995.

Rudnick, R. L., and D. M. Fountain, Nature and composition of the continental crust: a lower crustal perspective, *Rev. Geophys.*, 33, 267–309, 1995.

Rudnick, R. L., and T. Presper, Geochemistry of intermediate to high-pressure granulites, in *Granulites and crustal evolution*, edited by D. Vielzeuf, and P. Vidal, pp. 523–550, Kluwer Acad., Norwell, Mass., 1990.

Stockhert, B, and J. Renner, Rheology of crustal rocks at ultrahigh pressure, in *When continents collide: geodynamics and geochemistry of ultrahigh pressure rocks*, edited by B. H. Hacker, and J.G. Liou, pp. 57–95, Kluwer Acad., Norwell, Mass., 1998.

Suyehiro, K., Takahashi N., Ariie, Y., Yokoi, Y., Hino, R., Shinohara, M., Kanazawa, T., Hirata, N., Tokuyama, H., Taira, A. Continental crust, crustal underplating, and low-Q upper mantle beneath an oceanic island arc, *Science*, 272, 390–392, 1996.

Taylor, S. R., The origin and growth of continents, Tectonophysics, 4, 17–34, 1967.

Taylor, G. I., The instability of liquid surfaces when accelerated in a direction perpendicular to their planes, *Proc. R. Soc. Lond.*, A 201, 192–196.

Turcotte, D. L., Geophysical processes influencing the lower continental crust, in *Properties and processes of Earth's lower crust*, edited by R. F. Mereu, S. Mueller, and D. M. Fountain, pp. 321–329, Geophys. Mon., Washington, D.C., 1989.

Turcotte, D. L., and G. Schubert, Geodynamics applications of continuum physics to geological problems, John Wiley & Sons, Inc., New York, 1982.

van der Hilst, R. D., S. Widiyantoro, K. C. Creager, and T. J. McSweeney, Deep subduction and aspherical variations in P-wavespeed at the base of Earth's mantle, in *The core-mantle boundary region*, edited by M. Gurnis, M. E. Wysession, E. Knittle, and B. A. Buffett, pp. 5–20, Am. Geophys. Union, Washington, D.C., 1998.

White, R. S., Westbrook, K., Fowler, S. R., Spence, G. D., Barton, P. J., Joppen, M., Morgan, J., Bowen, A. N., Prestcott, C., Bott, M. H. P., Hatton Bank (Northwest U.K.) continental margin structure, *Geophys. J. Royal Astr. Soc.*, 89, 265–272, 1987.

Whitehead, J. A., and D. S. Luther, Dynamics of laboratory diapir and plume models, *J. Geophys.*

Res., 80, 705–717, 1975.

Zehnder, Carolyn M., Mutter, John C., Buhl, Peter, Deep seismic and geochemical constraints on the nature of rift-induced magmatism during breakup of the North Atlantic, *Tectonophysics*, 173, 545–565, 1990.

Table 1. Bulk compositions of crustal and mantle materials considered in this study for determining the density contrast between the lower crust and mantle.

Table 2. Parameters used in the finite element calculations for determining instability times of a dense lower crust.

Figure 1. Bulk composition of contintental crust in terms of Mg# and SiO_2 content, compared to the fractionation trend for basalt. Mixing of end-member components from basalt fractionation (i.e. "basalt" and "granite") can produce the bulk continental crust composition (high Mg# andesite). Modified from Kelemen (1995).

Figure 2. Calculated densities (kg/m^3) for crustal compositions of (a) low pressure gabbro, (b) high pressure gabbro, (c) average granulite, (d) basalt, (e) olivine clinopyroxenite, and (f) arc gabbronorite using Connolly's (1990) subsolidus phase equilibria program (VERTEX) Holland and Powell's (1998) thermodynamic database. Major element chemistry for the compositions shown is listed in Table 1. The lowest temperature of equilibration was set at 800 °C.

Figure 3. Calculated density contrast (kg/m^3) between the crustal compositions shown in Figure 2 and a pyrolite bulk composition calculated at the same P-T conditions for (a) low pressure gabbro, (b) high pressure gabbro, (c) average granulite, (d) basalt, (e) olivine clinopyroxenite, and (f) arc gabbronorite. Shaded contours are shown only where the density contrast is positive, indicating the P-T conditions at which the crustal compositions are denser than the mantle.

Figure 4. Calculated density and mode for (a) olivine clinopyroxenite, (b) arc gabbronorite, (c) low pressure gabbro, and (d) average granulite overlying a pyrolite mantle composition for a "cold" 300 °C geotherm. The temperature profile used in the density calculations is shown along with the mantle adiabat (dashed line) extending to the surface, corresponding to a mantle potential temperature of 1300 °C. The bold solid curves show the density profile for the crust extending down to 2.0 GPa. The light dotted curve shows the pyrolite density extended to the surface. The calculated mode for the crust and mantle compositions have abbreviations: (**ol**) olivine, (**cpx**) clinopyroxene, (**opx**) orthopyroxene, (**plg**) plagioclase, (**sp**) spinel, (**gt**) garnet, (**ky**) kyanite, and (**qrtz**) quartz.

Figure 5. Calculated densities of all crustal and mantle compositions along a 300 °C geotherm. Crustal densities are shown extending down to a pressure of 2.0 GPa. Densities for pyrolite (thin dashed curve), abyssal peridotite (thin dotted curve), and cratonic peridotite (thin solid curve) are shown over the entire pressure range.

Figure 6. Calculated densities for crustal and mantle compositions corresponding to "hot" 800 °C and 1000 °C geotherms. The grey horizontal line in the density plots marks the pressure at which the conductive temperature profile intersects the adiabat. The density of the high and low P gabbros are significantly reduced at these higher temperatures, while the arc gabbronorite and basalt compositions have densities that are very sensitive to small changes in temperature and pressure.

Figure 7. Density profile of the arc gabbronorite composition during cooling from a 1000 °C geotherm to a 800 °C geotherm. Time intervals are shown in Myr, starting at 0 Myr for the initial 1000 °C profile, with cooling almost complete in 10.2 Myr. The arc gabbronorite composition (b) extends down to the pressure where the 800 °C geotherm intersects the adiabat (dashed grey line). Densities for pyrolite (thin black curve) and cratonic peridotite (thin grey curve) mantle compositions are shown for reference.

Figure 8. Effective viscosities calculated for the phases listed in Table 2, undergoing dislocation creep at differential stress of 0.1 to 100 MPa at temperatures of (a) 600 °C, (b) 900 °C, and (c) 1200 °C.

Figure 9. Schematic illustration of the crust and mantle showing parameters governing the development of convective instability. The upper crustal layer has a density ρ_2, stress exponent n_2, and rheological coefficient B_2. The dense lower crustal layer has a thickness h, density ρ_1, stress exponent n_1, and rheological coefficient B_1. The mantle has a density ρ_0, stress exponent n_0,

and rheological coefficient B_0. The dense layer is initially displaced with a sinusoidal perturbation with wavelength λ and amplitude Z_0 to initiate the development of the instability. The upper crustal layer is neutrally buoyant and serves to decouple the dense layer from the rigid surface.

Figure 10. (a) Development of a convective (Rayleigh-Taylor) instability for a dense layer (dark shaded region) overlying a less dense mantle with a Newtonian viscosity. Initially the dense layer is perturbed at the the bottom with a wavelength equal to twice the horizontal extent of the dense layer. With time the fastest growing wavelength of the instability dominates. (b) Time series of the development of an instability for a dense layer overlying a less dense mantle. Initially the interface is deflected by 1 % of the dense layer thickness, with a maximum amplitude on the left side. For a non-Newtonian viscosity the planform of the instability is nearly identical, but the time scale is different. The growth of the instability is tracked by following the displacement of the bottom of the dense layer at the left-hand side.

Figure 11. Vertical displacement (solid dark curves) during the growth of an instability for (a) Newtonian and (b) non-Newtonian viscosities. A Newtonian viscosity causes steady and continuous exponential growth of the instability, while a non-Newtonian viscosity causes super-exponential growth that is initially very slow. The grey curves show the result of taking $\ln(Z)$ for the Newtonian result and $Z^{(1-n)}$ for the non-Newtonian results. See text for explanation.

Figure 12. Calculated growth rates (q') as a function of wavenumber ($k' = 2\pi/\lambda'$) for a Newtonian viscosity with strong ($\eta_1/\eta_0 = 1$) and weak ($\eta_1/\eta_0 = 0.01$) dense lower crustal layers and a mantle with several different decay lengths (L/h) for the rheological coefficient (B_0). Shown are results from finite element two-dimensional calculations (data points) and linear analysis (continuous curves). In (a), the dense layer is “strong” and has a viscosity equal to that at the top of the mantle. In (b), the dense layer is “weak” and has a viscosity that is two orders of magnitude less

than the top of the mantle.

Figure 13. (a) Maximum growth rates (q'_{max}) and (b) wavenumbers (k'_{max}) for a strong and weak dense lower crustal layer with a non-Newtonian viscosity and a range of decay lengths for the rheological coefficient in the mantle. Limiting cases are: 1) the decay length of the rheological coefficient in the mantle is much larger than the dense layer thickness ($L >> h$), so that viscosity in the mantle is nearly constant, and 2) the viscous decay length of the mantle is much shorter than the dense layer thickness ($L << h$) so that the viscosity of the dense layer controls the growth rate of the instability. The results from Figure 12 are also shown as symbols ($\oplus$).

Figure 14. Instability time calculated from equation (10) as a function of Moho temperature for a Newtonian viscosity with four different profiles: (a) strong dense layer over a constant B_0 mantle, (b) weak dense layer over a constant B_0 mantle, (c) strong dense layer over a mantle with an exponentially decreasing B_0, and (d) weak dense layer over a mantle with an exponentially decreasing B_0. Results are shown for 10 and 1 km dense layer thickness (dark and light shaded regions) and with density contrasts of 50, 100, and 200 kg/m^3 (labelled curves). Intersection of the calculated instability times with the horizontal grey line gives the Moho temperature required for the instability to develop in 10 Myr (shown as light grey shaded bars).

Figure 15. Calculated growth rate factor (C) as a function of wavenumber ($k' = 2\pi/\lambda'$) for strong ($B_1/B_0 = 1$) and weak ($B_1/B_0 = 0.01$) dense lower crustal layers with a non-Newtonian viscosity and a mantle with several different viscous decay lengths (L/h). If $L >> h$, the viscosity of the mantle is nearly constant, while if $L/h > 1.158$, the viscosity of dense layer dominates the growth of an instability.

Figure 16. Instability times calculated from equation (12) as a function of Moho temperature for

a non-Newtonian viscosity with four different profiles: (a) strong dense layer over a constant B_0 mantle, (b) weak dense layer over a constant B_0 mantle, (c) strong dense layer over a mantle with exponentially decreasing B_0, and (d) weak dense layer over a mantle with exponentially decreasing B_0. Results are shown for 10 and 1 km dense layer thickness (dark and light shaded regions) and with density contrasts of 50, 100, and 200 kg/m^3 (labelled curves). Intersection of the calculated instability times with the horizontal grey line gives the Moho temperature required for the instability to develop in 10 Myr (shown as light grey shaded bars).

Figure 17. Non-dimensional instability time (t_b') as a function of non-dimensional horizontal strain rate ($\dot{\epsilon}'$) for strong and weak dense lower crustal layers with non-Newtonian viscosity. With small initial horizontal strain rates, instability times are unchanged. After reaching a critical initial horizontal strain rates that varies for the strong and weak dense layers, instability times decrease because the initial effective viscosity is lower.

Figure 18. Instability times with initial horizontal strain rates of 10^{-18} s^{-1} and 10^{-14} s^{-1}, and without any initial horizontal strain rate. Column (a) shows results for a 1 km thick dense layer and column (b) for a 10 km thick dense layer with both constant and exponentially decreasing B_0. Intersection of the horizontal grey lines with the calculated instability times give Moho temperatures required for 10 Myr instabilities to develop from 1% and 100% initial deflections.

Figure 19. Density profiles calculated for a pyrolite mantle composition using Holland and Powell's (1998) and Berman's (1996) thermodynamic databases along a 300 °C geotherm extending down to a pressure of 6 GPa. In (b) the calculated density profile using Holland and Powell's (1998) database has a positive slope (solid curve) and is gravitationally "stable", while the density profile calculated using Berman's (1996) database (dashed curve) has a negative slope and is "unstable". The reason for this is evident from the different values for bulk expansivity (c) and

compressibility (d) calculated from these two databases.

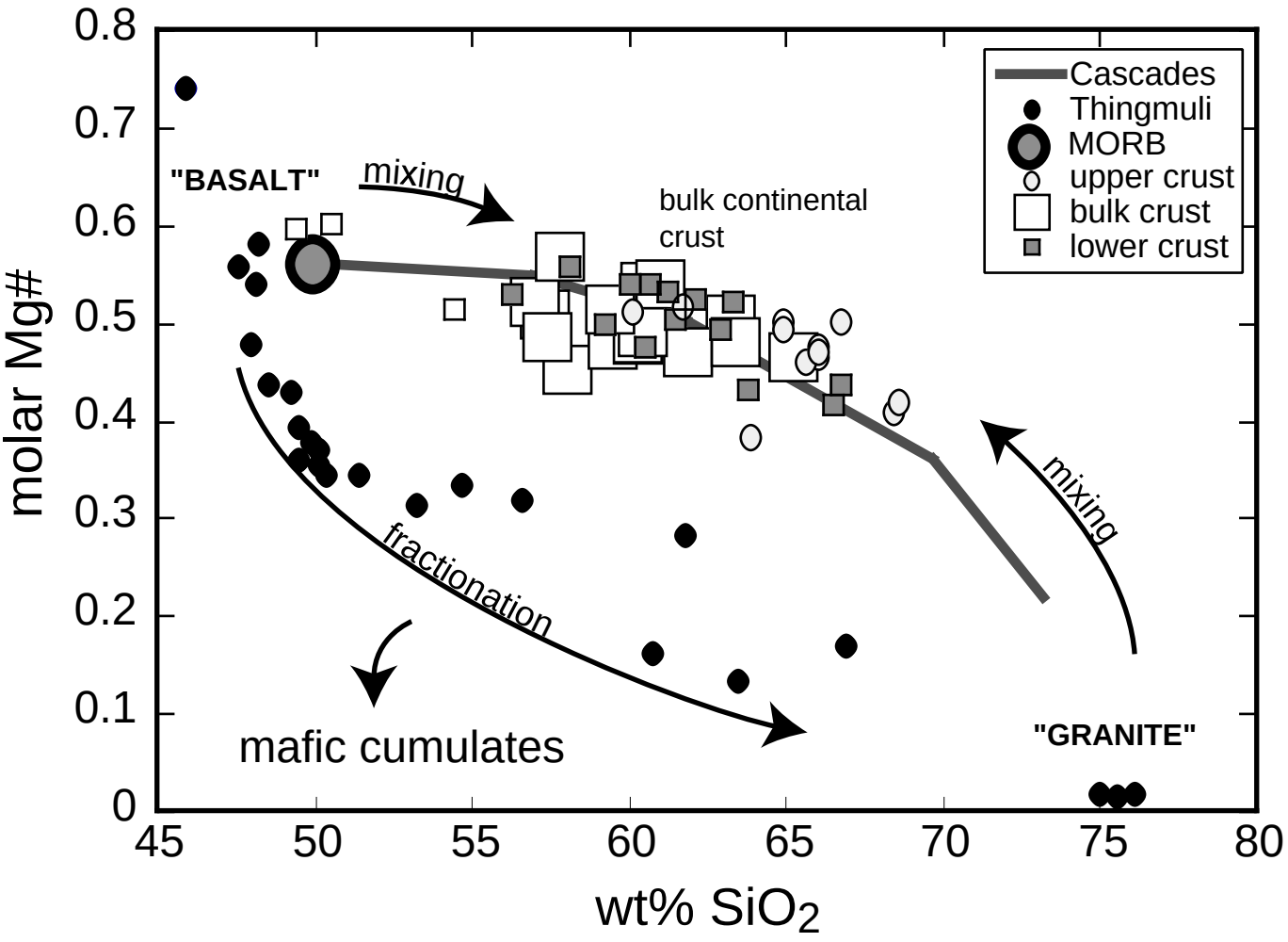
0.8
0.7
0.6
0.5
0.4
0.3
0.2
0.1
0
molar Mg#
45
50
55
60
65
70
75
80
wt% SiO2
Cascades
Thingmuli
MORB
upper crust
bulk crust
lower crust
"BASALT"
mixing
bulk continental crust
mixing
fractionation
mafic cumulates
"GRANITE"

Figure 1.

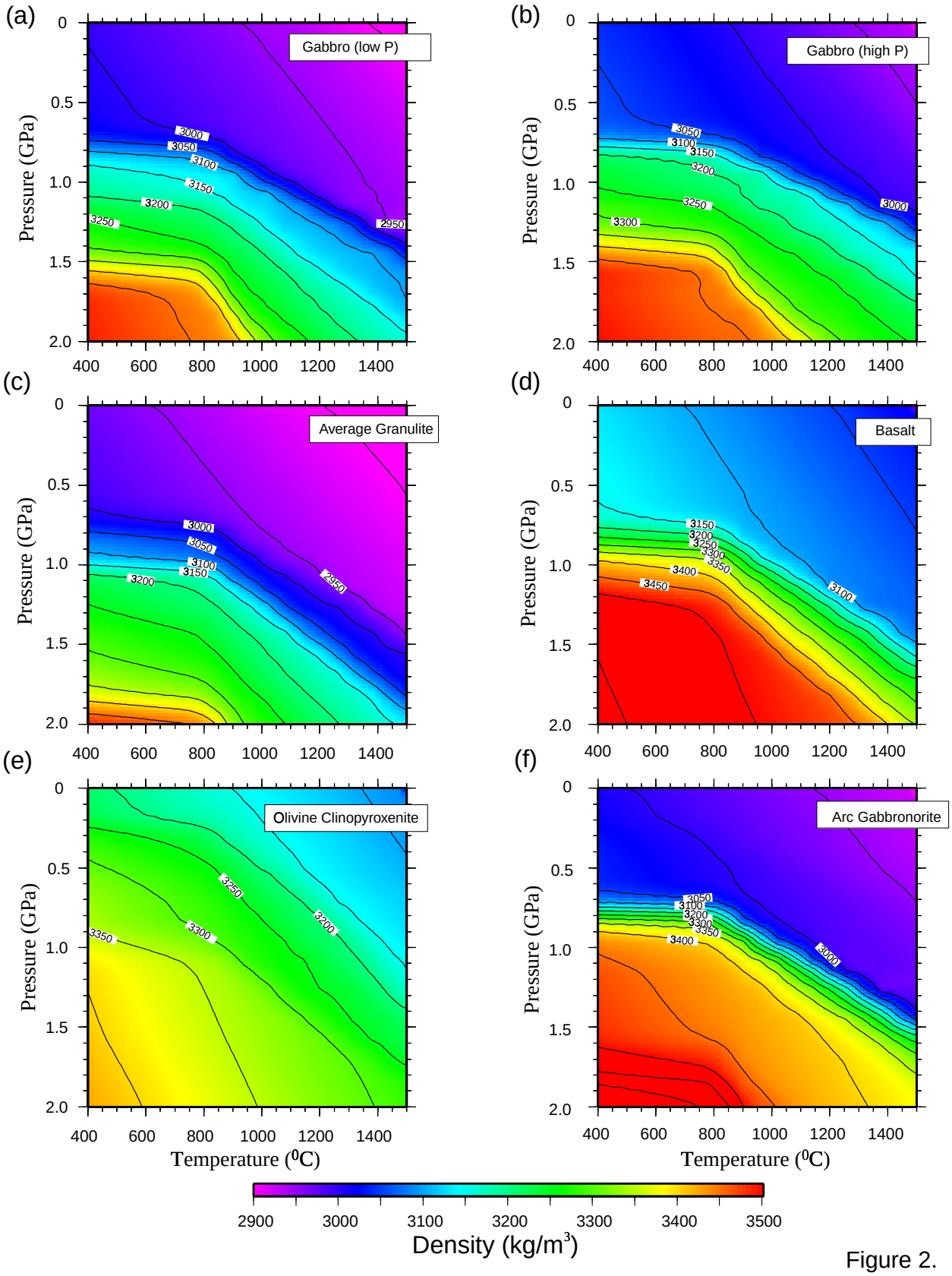
(a)
Gabbro (low P)
(b)
Gabbro (high P)
(c)
Average Granulite
(d)
Basalt
(e)
Olivine Clinopyroxenite
(f)
Arc Gabbronorite
Pressure (GPa)
Temperature (0C)
Density (kg/m3)

Figure 2.

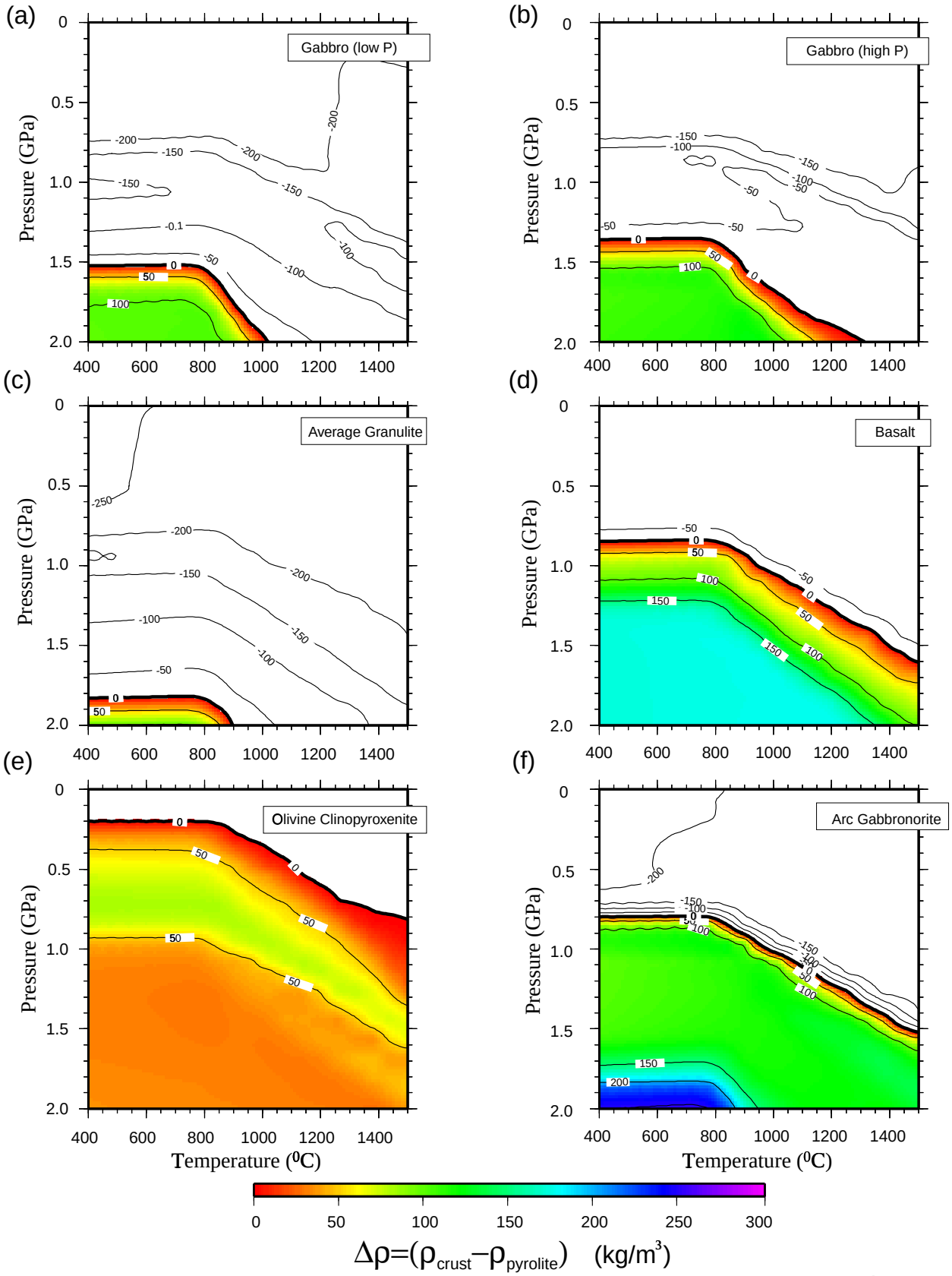
(a)
Gabbro (low P)
(b)
Gabbro (high P)
(c)
Average Granulite
(d)
Basalt
(e)
Olivine Clinopyroxenite
(f)
Arc Gabbronorite
Pressure (GPa)
Temperature (⁰C)
0
0.5
1.0
1.5
2.0
400
600
800
1000
1200
1400
0
50
100
150
200
250
300
Δρ=(ρcrust−ρpyrolite) (kg/m3)

Figure 3.

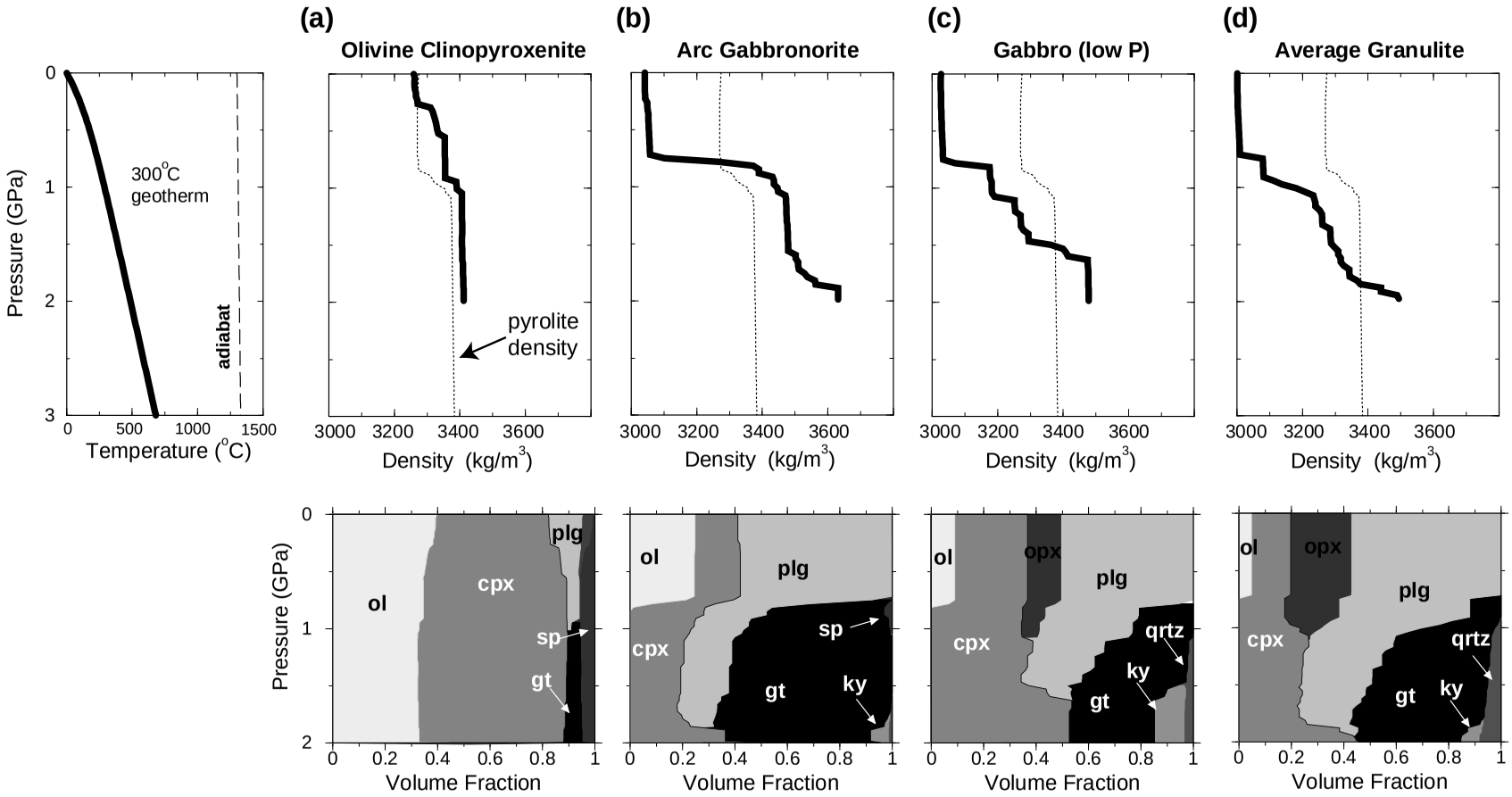
(a)
Olivine Clinopyroxenite
(b)
Arc Gabbronorite
(c)
Gabbro (low P)
(d)
Average Granulite
Pressure (GPa)
300°C
geotherm
adiabat
Temperature (°C)
pyrolite
density
Density (kg/m3)
ol
cpx
plg
sp
gt
opx
ky
qrtz
Volume Fraction

Figure 4.

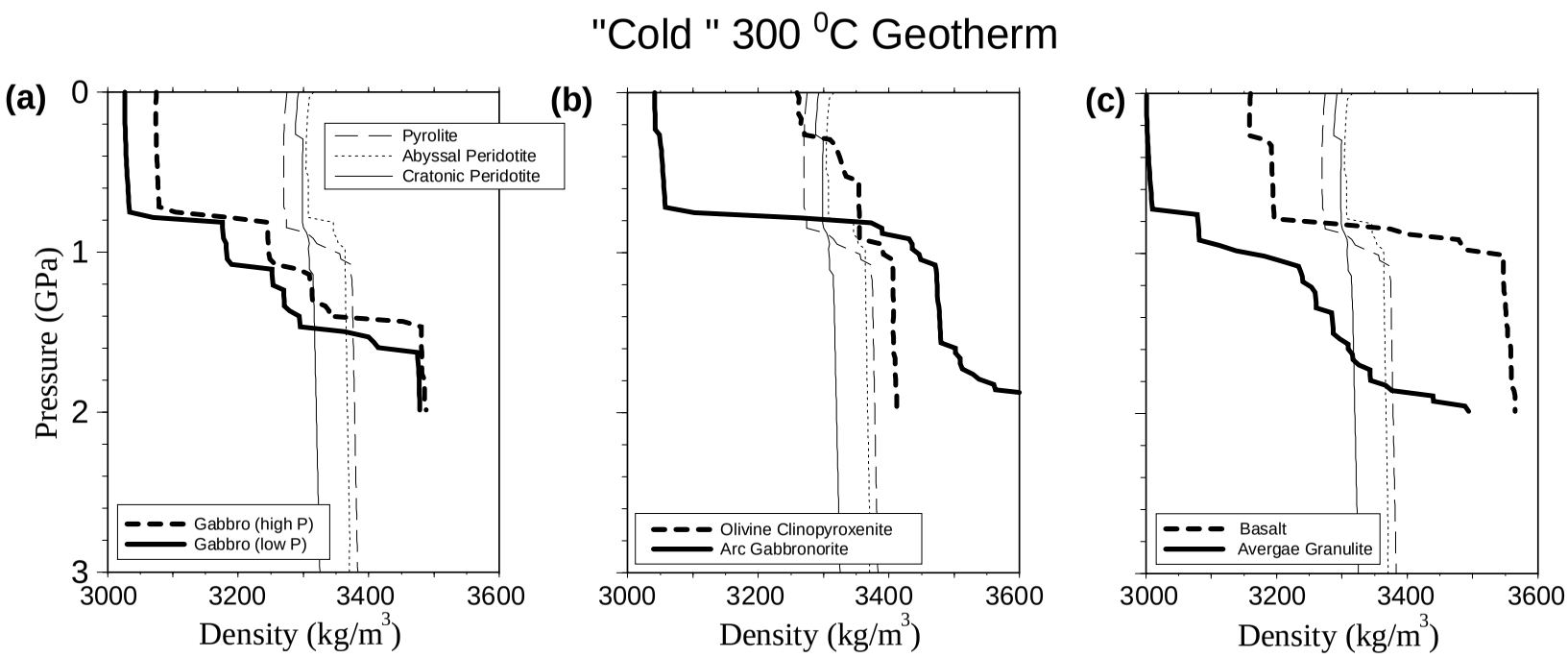
"Cold " 300 0C Geotherm
(a)
(b)
(c)
Pressure (GPa)
0
1
2
3
Pyrolite
Abyssal Peridotite
Cratonic Peridotite
Gabbro (high P)
Gabbro (low P)
Olivine Clinopyroxenite
Arc Gabbronorite
Basalt
Avergae Granulite
3000
3200
3400
3600
Density (kg/m3)

Figure 5

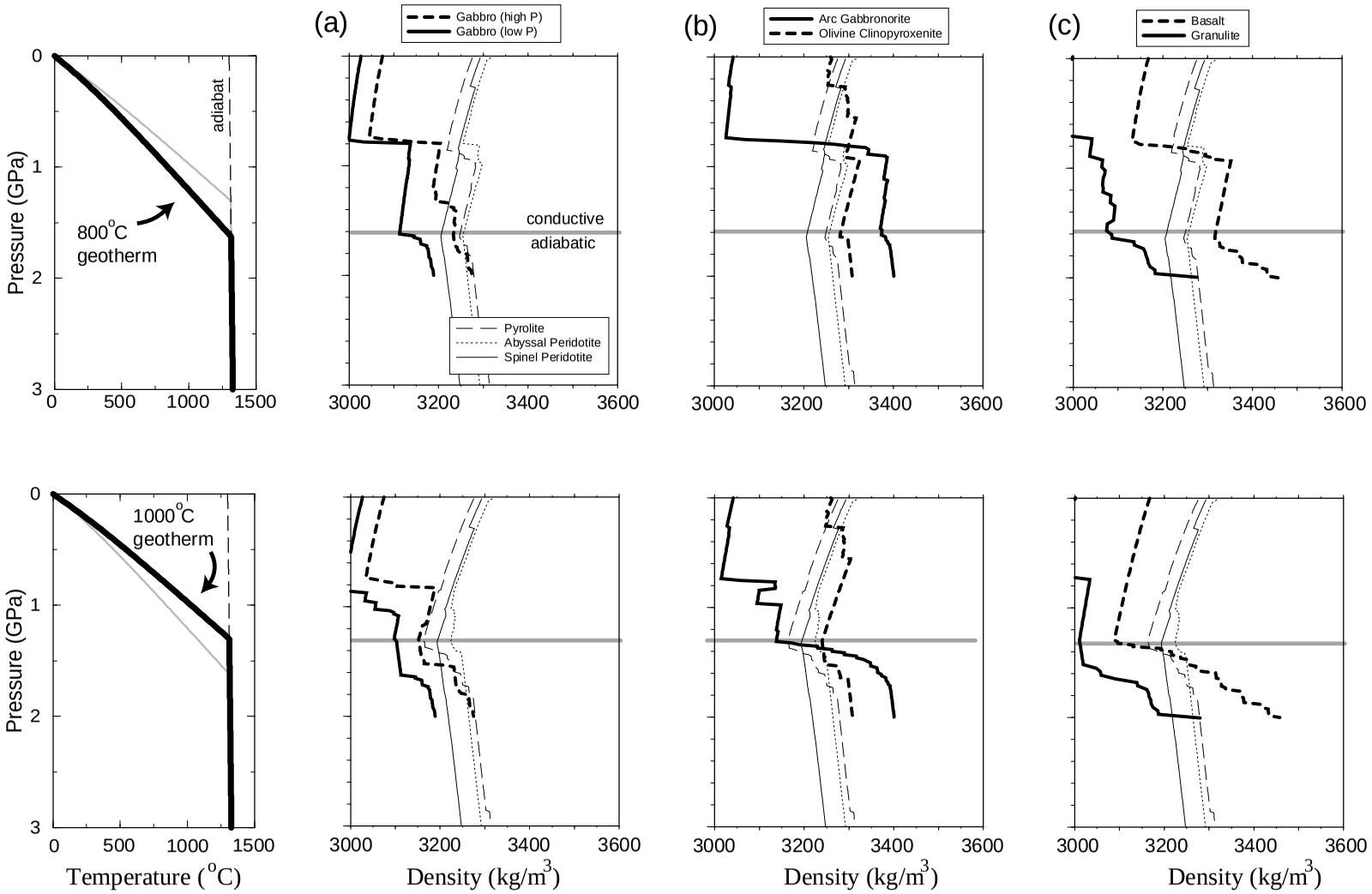
(a)
(b)
(c)
Gabbro (high P)
Gabbro (low P)
Arc Gabbronorite
Olivine Clinopyroxenite
Basalt
Granulite
adiabat
800°C
geotherm
1000°C
geotherm
conductive
adiabatic
Pyrolite
Abyssal Peridotite
Spinel Peridotite
Pressure (GPa)
Temperature (°C)
Density (kg/m3)
0
1
2
3
0
500
1000
1500
3000
3200
3400
3600

Figure 6

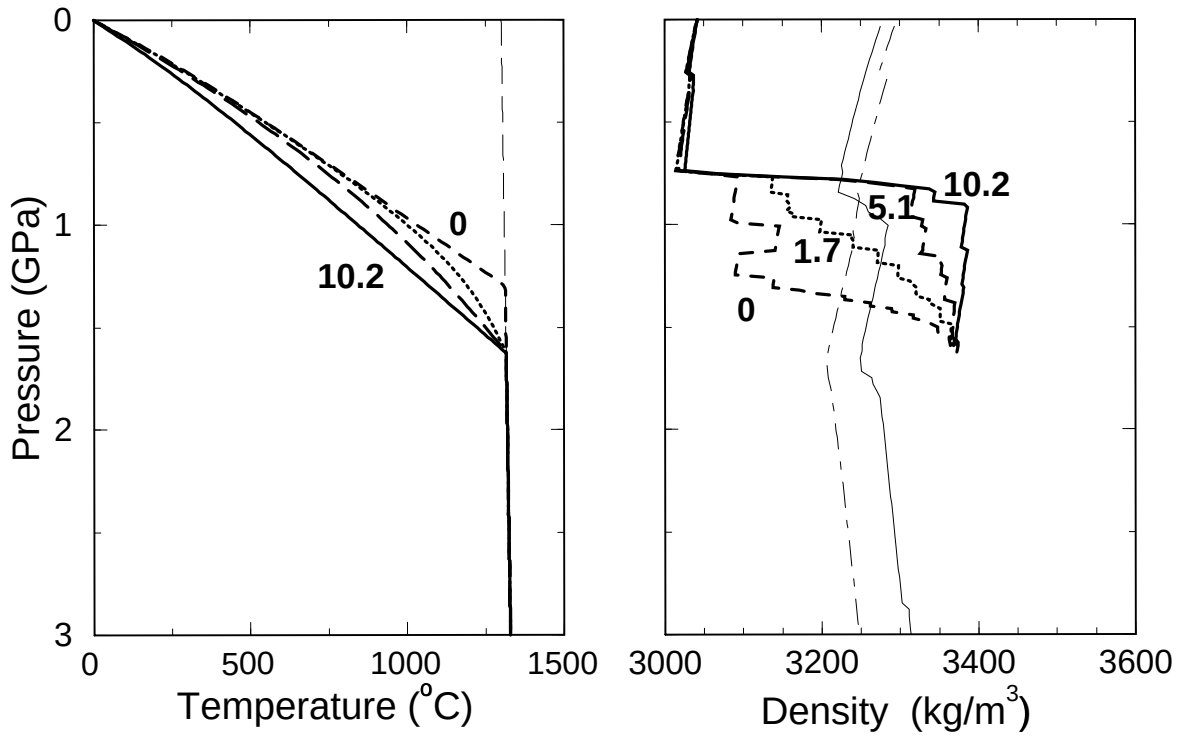
0
1
2
3
Pressure (GPa)
0
500
1000
1500
Temperature (°C)
0
10.2
3000
3200
3400
3600
Density (kg/m3)
10.2
5.1
1.7
0

Figure 7

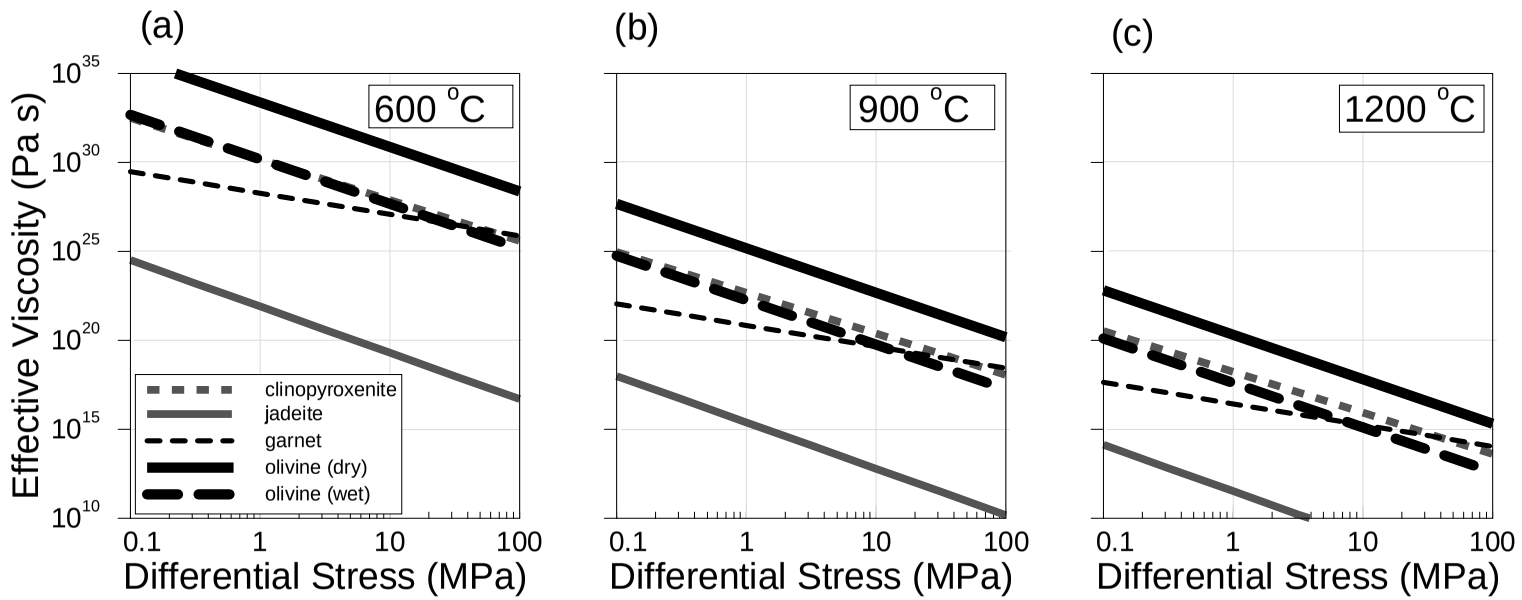
(a)
(b)
(c)
600 °C
900 °C
1200 °C
Effective Viscosity (Pa s)
10^35
10^30
10^25
10^20
10^15
10^10
clinopyroxenite
jadeite
garnet
olivine (dry)
olivine (wet)
0.1
1
10
100
Differential Stress (MPa)

Figure 8

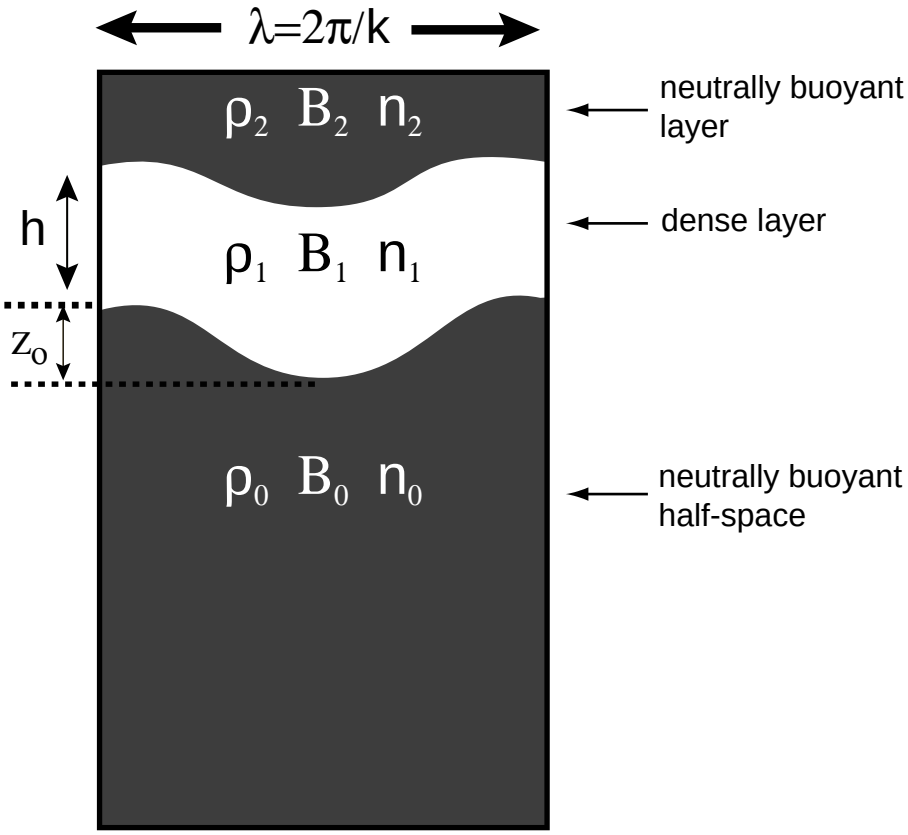
λ=2π/k
ρ2 B2 n2
neutrally buoyant layer
h
ρ1 B1 n1
dense layer
zo
ρ0 B0 n0
neutrally buoyant half-space

Figure 9

(a)

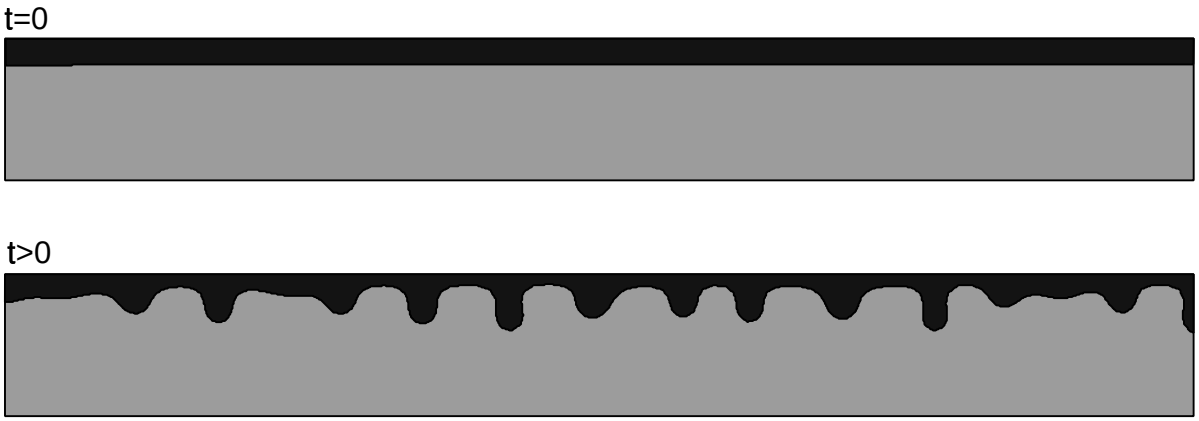

(b)

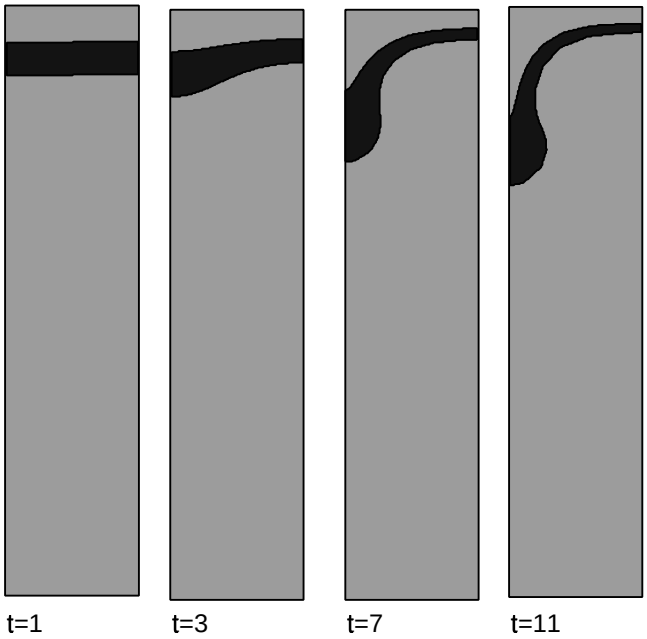

Figure 10

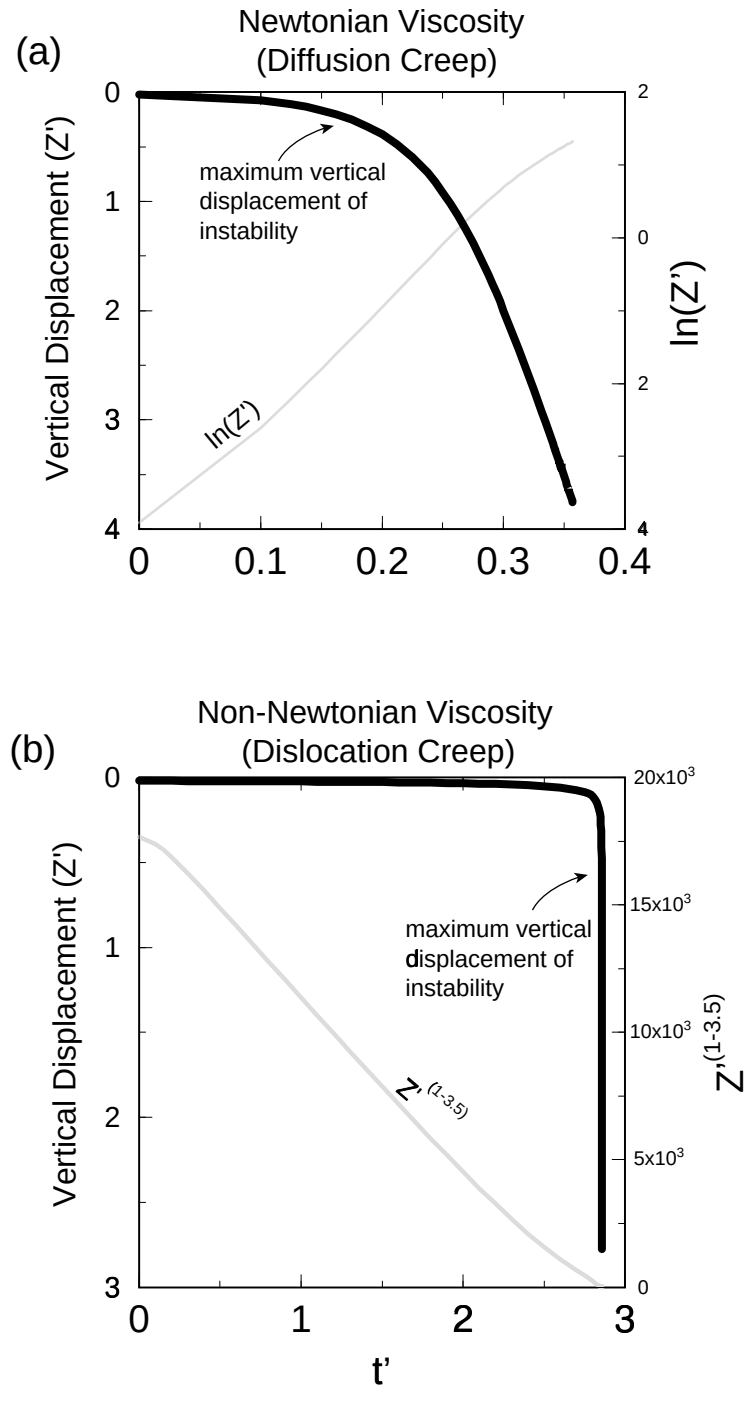
(a)
Newtonian Viscosity
(Diffusion Creep)
Vertical Displacement (Z')
ln(Z')
maximum vertical
displacement of
instability
ln(Z')
0
1
2
3
4
0
0.1
0.2
0.3
0.4
2
0
2
4
(b)
Non-Newtonian Viscosity
(Dislocation Creep)
Vertical Displacement (Z')
maximum vertical
displacement of
instability
Z'(1-3.5)
Z'(1-3.5)
0
1
2
3
t'
20x10^3
15x10^3
10x10^3
5x10^3
0

Figure 11.

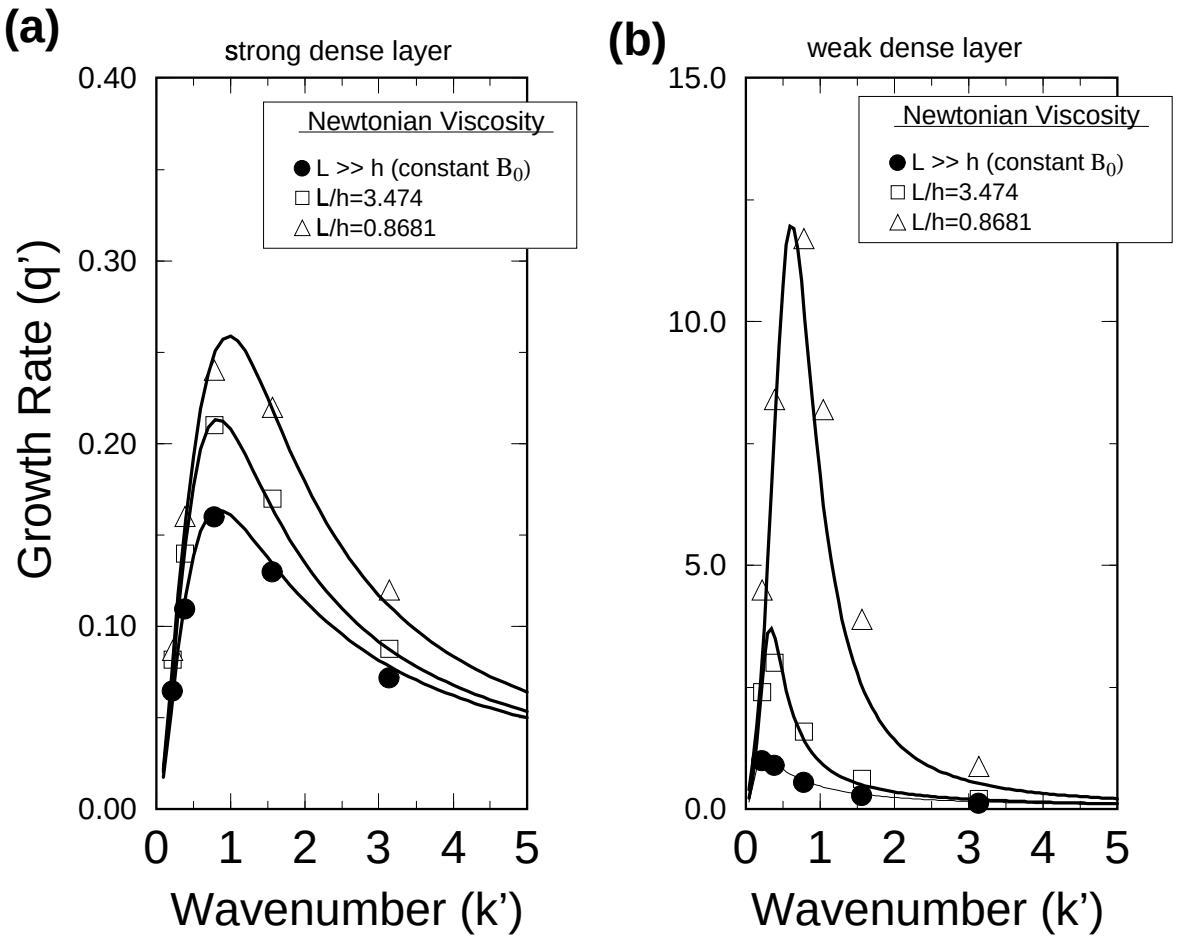
(a)
strong dense layer
Newtonian Viscosity
L >> h (constant B0)
L/h=3.474
L/h=0.8681
Growth Rate (q')
Wavenumber (k')
0.00
0.10
0.20
0.30
0.40
0 1 2 3 4 5
(b)
weak dense layer
Newtonian Viscosity
L >> h (constant B0)
L/h=3.474
L/h=0.8681
0.0
5.0
10.0
15.0
0 1 2 3 4 5
Wavenumber (k')

Figure 12

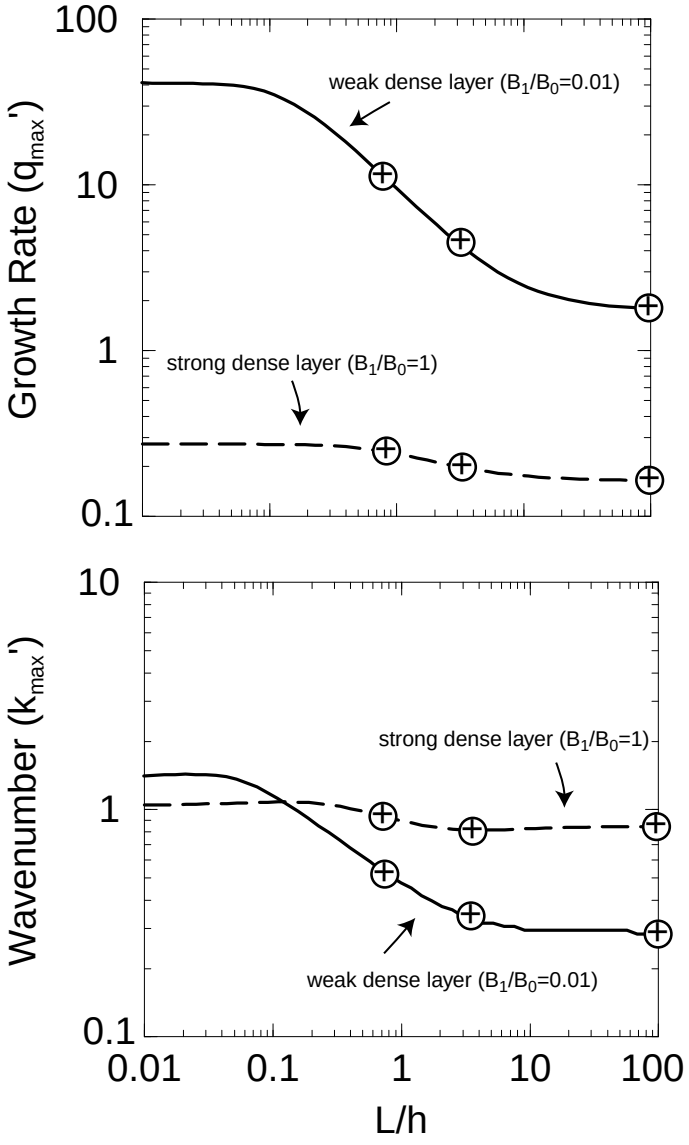
100
10
1
0.1
Growth Rate (q_{max}')
weak dense layer (B_1/B_0=0.01)
strong dense layer (B_1/B_0=1)
10
1
0.1
Wavenumber (k_{max}')
strong dense layer (B_1/B_0=1)
weak dense layer (B_1/B_0=0.01)
0.01
0.1
1
10
100
L/h

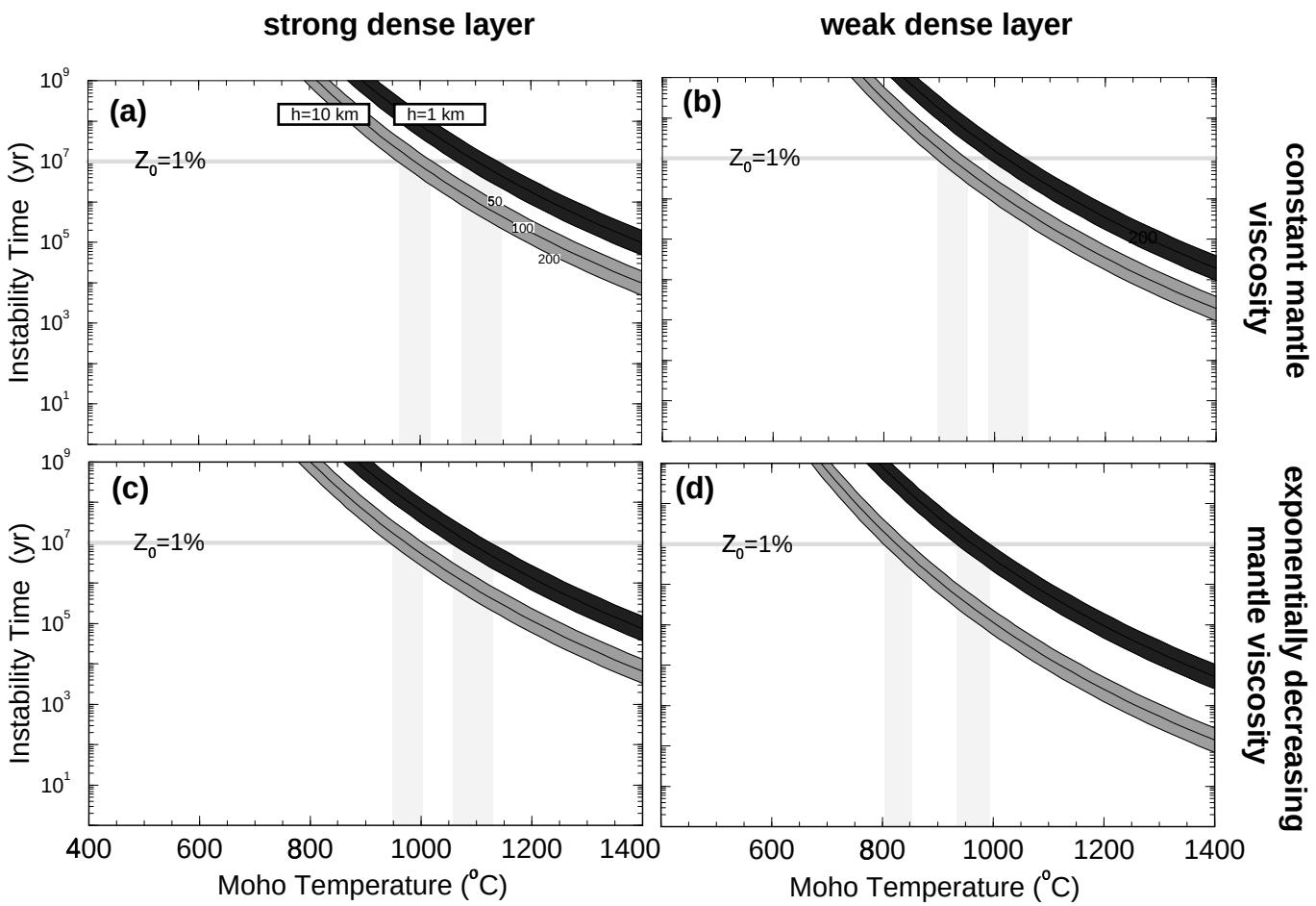
strong dense layer
weak dense layer
constant mantle viscosity
exponentially decreasing mantle viscosity
(a)
(b)
(c)
(d)
h=10 km
h=1 km
Z_0=1%
50
100
200
Instability Time (yr)
Moho Temperature (°C)
400
600
800
1000
1200
1400
10^1
10^3
10^5
10^7
10^9

Figure 14

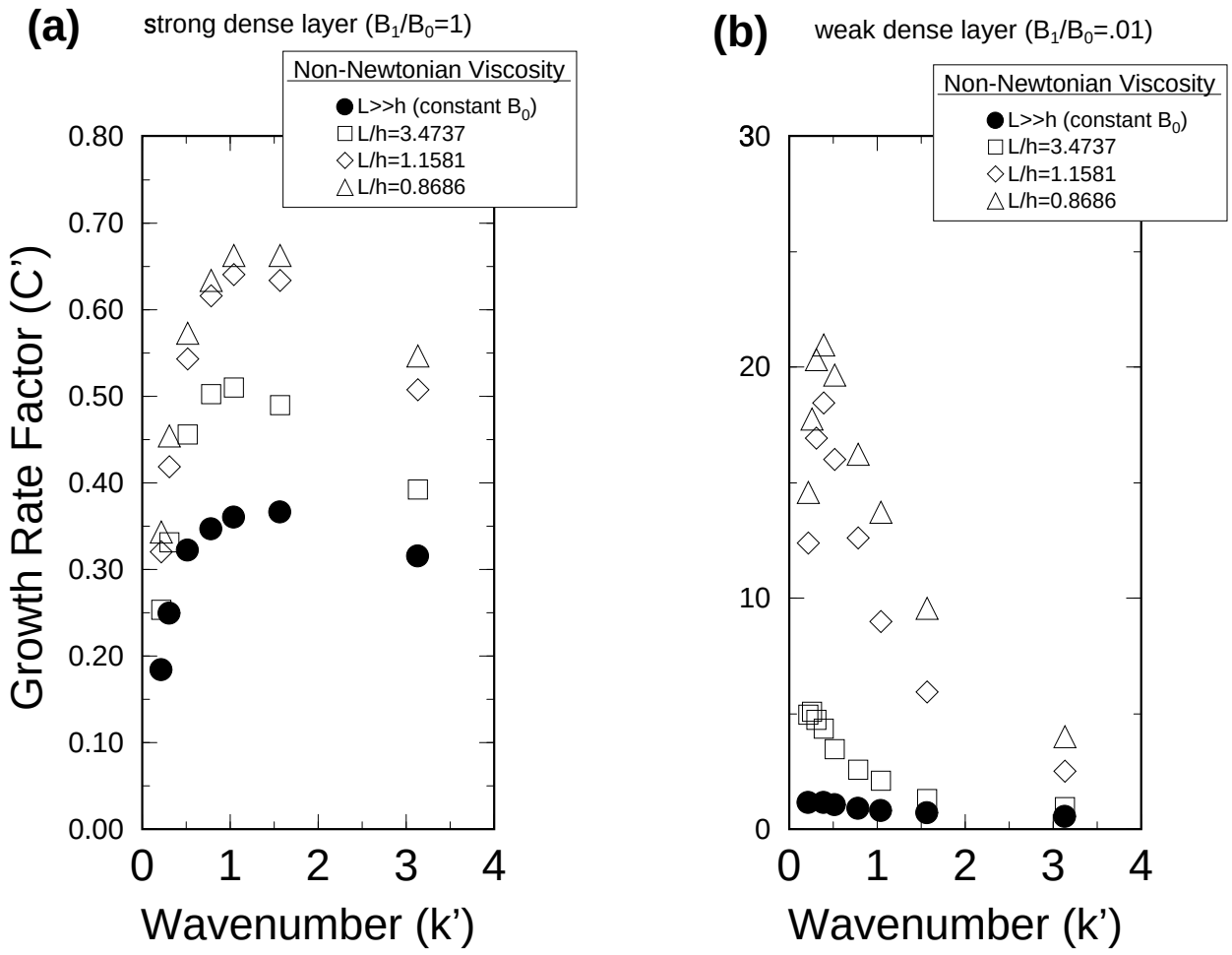
(a)
strong dense layer (B_1/B_0=1)
Non-Newtonian Viscosity
L>>h (constant B_0)
L/h=3.4737
L/h=1.1581
L/h=0.8686
Growth Rate Factor (C')
Wavenumber (k')
0.00
0.10
0.20
0.30
0.40
0.50
0.60
0.70
0.80
0
1
2
3
4
(b)
weak dense layer (B_1/B_0=.01)
Non-Newtonian Viscosity
L>>h (constant B_0)
L/h=3.4737
L/h=1.1581
L/h=0.8686
Wavenumber (k')
0
10
20
30
0
1
2
3
4

Figure 15

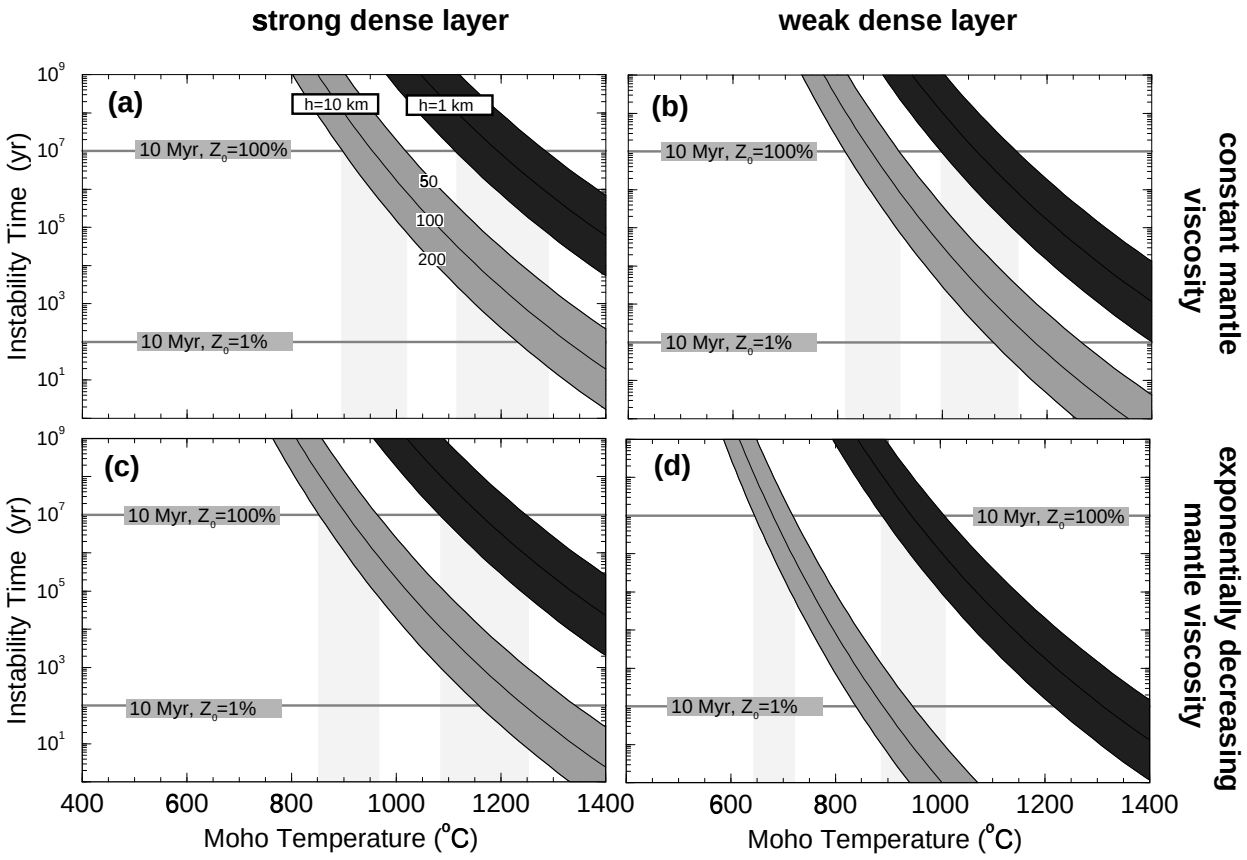
strong dense layer
weak dense layer
constant mantle viscosity
exponentially decreasing mantle viscosity
(a)
(b)
(c)
(d)
h=10 km
h=1 km
50
100
200
10 Myr, Z0=100%
10 Myr, Z0=1%
Instability Time (yr)
Moho Temperature (°C)
400
600
800
1000
1200
1400

Figure 16

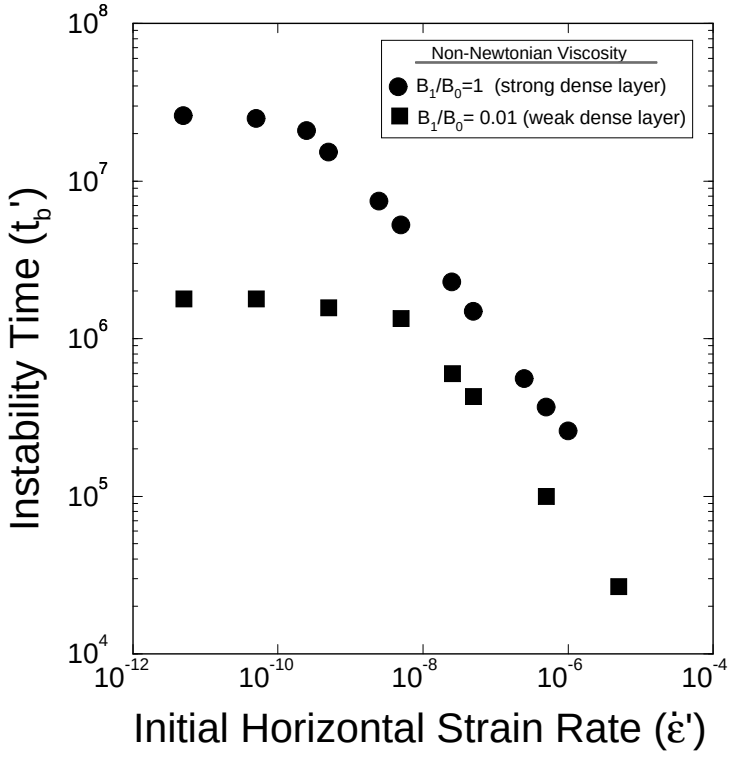
Non-Newtonian Viscosity
B1/B0=1 (strong dense layer)
B1/B0= 0.01 (weak dense layer)
Instability Time (tb')
Initial Horizontal Strain Rate (ε̇')
10^8
10^7
10^6
10^5
10^4
10^-12
10^-10
10^-8
10^-6
10^-4

Figure 17

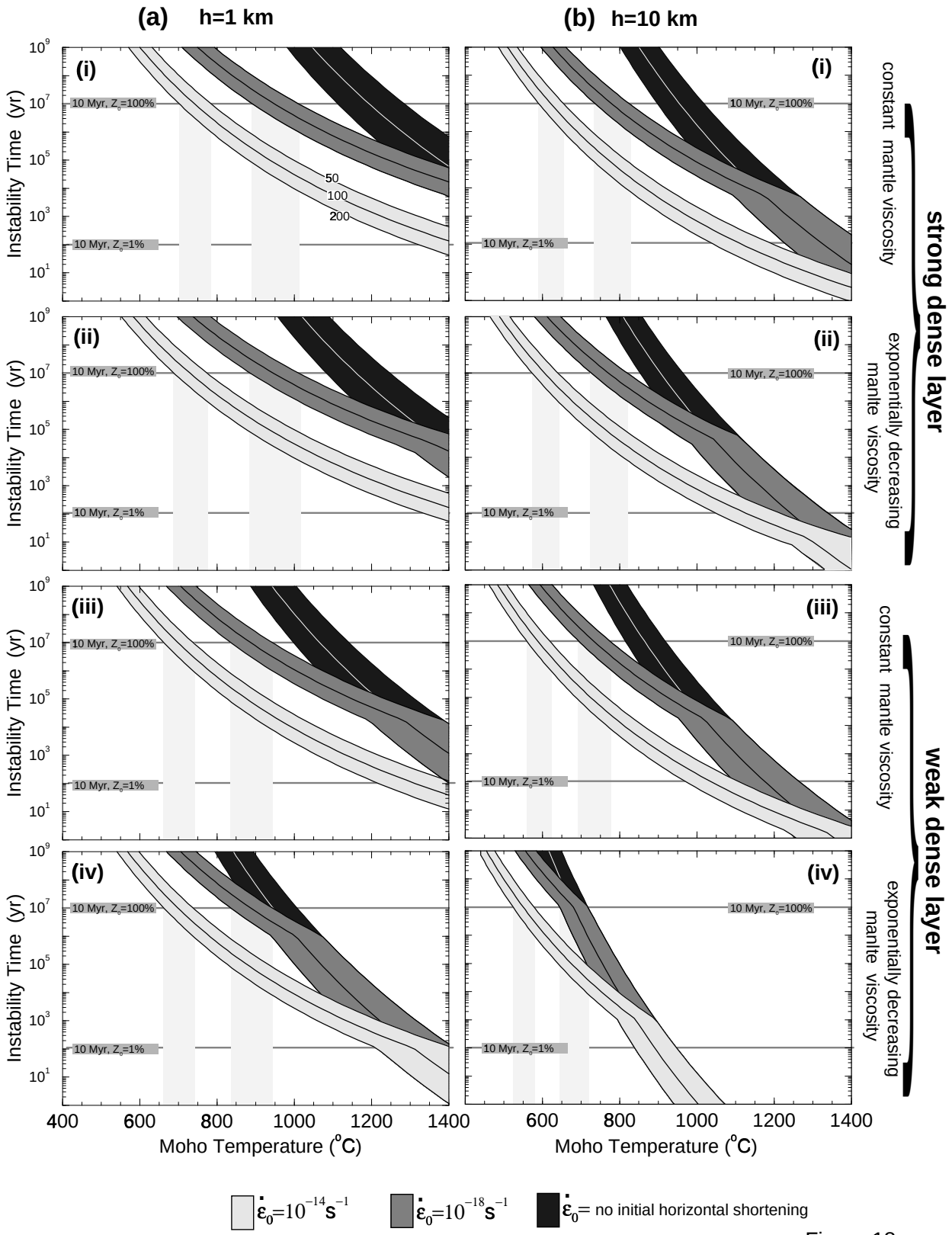
(a) h=1 km
(b) h=10 km
(i)
(ii)
(iii)
(iv)
10 Myr, Z0=100%
10 Myr, Z0=1%
50
100
200
Instability Time (yr)
Moho Temperature (°C)
strong dense layer
weak dense layer
constant mantle viscosity
exponentially decreasing manlte viscosity
ε̇0=10−14s−1
ε̇0=10−18s−1
ε̇0= no initial horizontal shortening

Figure 18

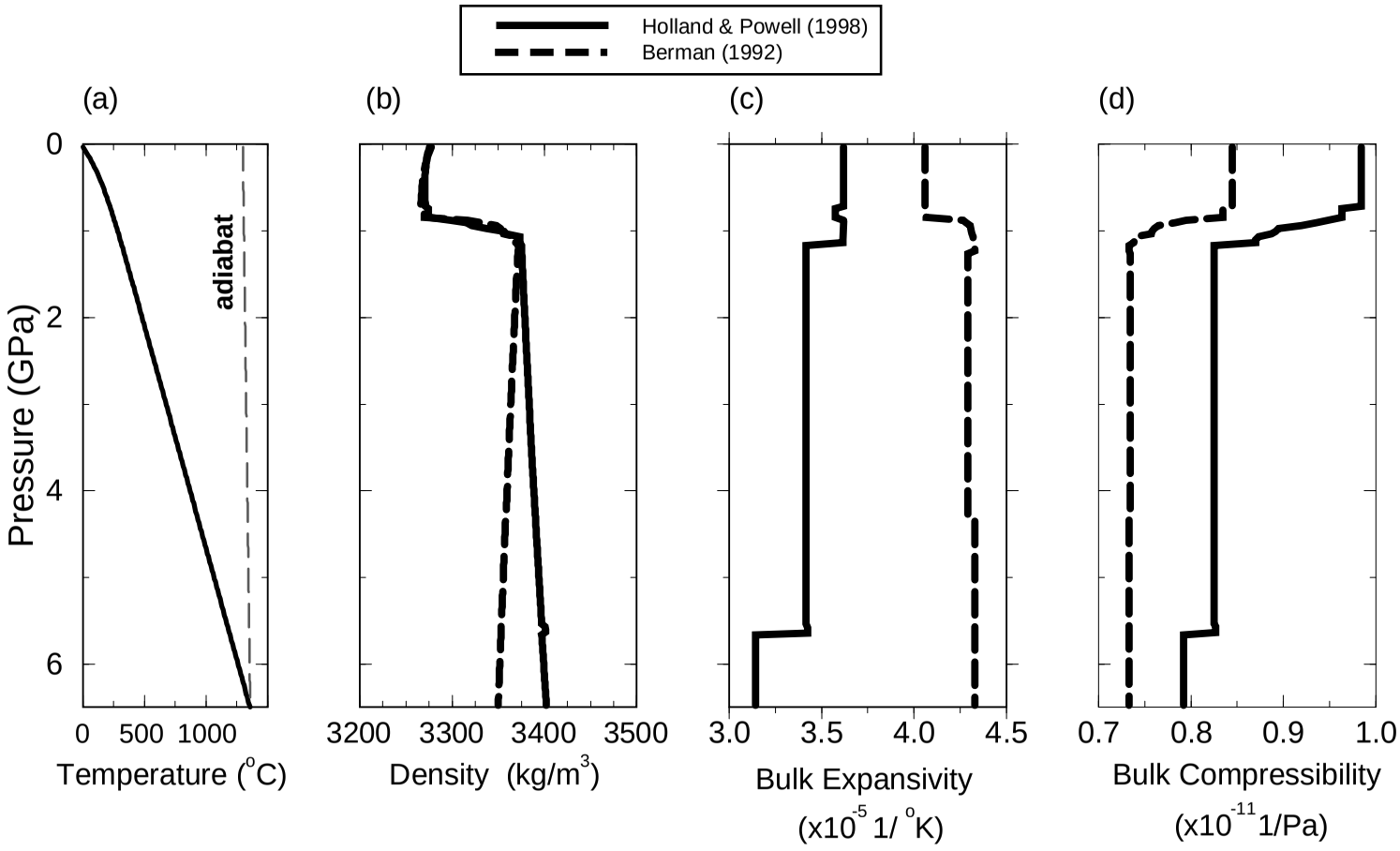
Holland & Powell (1998)
Berman (1992)
(a)
(b)
(c)
(d)
Pressure (GPa)
0
2
4
6
adiabat
0 500 1000
Temperature (°C)
3200 3300 3400 3500
Density (kg/m3)
3.0 3.5 4.0 4.5
Bulk Expansivity
(x10-5 1/ °K)
0.7 0.8 0.9 1.0
Bulk Compressibility
(x10-11 1/Pa)

Figure 19

Table 1: Major Element Analyses

	SiO_2	TiO_2	Al_2O_3	FeO	MnO	MgO	CaO	Na_2O	K_2O	P_2O_5	Cr_2O_3	NiO	Mg#
Crust Compositions													
Gabbro (Low P)[a]	49.90	0.31	16.89	6.00	—	10.50	14.60	1.50	0.03	—	—	—	75.73
Gabbro (High P)[b]	48.49	0.61	15.87	5.12	0.03	12.52	16.64	0.50	0.10	—	—	—	81.34
Olivine Clinopyroxenite[c]	44.55	0.61	6.76	7.88	0.17	22.95	12.22	1.26	0.43	—	—	—	83.85
Arc Gabbronorite[d]	45.66	0.86	19.26	11.53	—	7.69	12.88	1.74	0.07	—	—	—	54.31
Granulite[e]	49.36	0.91	16.72	8.78	0.14	7.32	10.36	2.45	0.40	0.13	—	—	59.78
Basalt[f]	47.50	1.85	10.89	12.26	0.20	16.05	9.26	1.67	0.15	0.20	—	—	70.00
Mantle Compositions													
Pyrolite[g]	45.10	0.20	3.30	8.00	0.15	38.10	3.10	0.40	0.03	—	0.40	—	89.46
Cratonic Peridotite[h]	42.63	0.01	0.82	6.65	0.19	48.43	0.19	0.03	—	—	0.72	0.33	92.84
Abyssal Peridotite[i]	43.65	0.03	1.96	8.43	0.14	42.87	1.99	0.05	0.01	—	0.36	0.22	90.06

[a]Oman ophiolite low pressure gabbro (Pallister, 1984)
[b]East Greenland high pressure gabbro (Bernstein, 1994)
[c]Aleutian ultramafic xenolith (Conrad and Kay, 1984)
[d]Tonsina arc section gabbronorite (Burns, 1983)
[e]Average granulite xenolith (Rudnick and Presper, 1990)
[f]East Greenland (calculated) primary basalt (Fram and Lesher,1997)
[g]Inferred primitive mantle (Ringwood, 1979)
[h]East Greenland harzburgite xenolith (Bernstein et al., 1998)
[i]Southern mid-Atlantic ridge dredge sample of depleted peridotite (Dick, 1989)

Table 2: Rheological Parameters

	n	m	ln(A[$MPa^{-n}s^{-1}$])	Q (kJ/mol)	
DISLOCATION CREEP					
clinopyroxenite	3.3 ± 0.9	0	11.9	490 ± 159	Boland and Tullis (1986)
jadeite	3.6 ± 0.3	0	22 ± 2	425 ± 25	Stockhert and Renner (1998)
garnet	2.2 ± 0.1	0	15.6	485 ± 30	Ji and Martignole (1994)
olivine (dry)	3.5	0	10.8 ± 2	535 ± 30	Hirth and Kohlstedt (1996)
olivine (wet)	3.5	0	15.4 ± 2	515 ± 30	Hirth and Kohlstedt (1996)
DIFFUSION CREEP					
olivine (dry)	1	-3	16.7	315 ± 35	Hirth and Kohlstedt (1996)